THE ASTROPHYSICAL JOURNAL, 357:71–90, 1990 July 1

SURFACE PHOTOMETRY OF BARRED SPIRAL GALAXIES

KOUJI OHTA
Department of Astronomy, Faculty of Science, Kyoto University
MASARU HAMABE
Kiso Observatory, Institute of Astronomy, The University of Tokyo
AND
KEN-ICHI WAKAMATSU[1,2]
Physics Department, College of Technology, Gifu University
Received 1989 September 5; accepted 1990 January 2

ABSTRACT

Detailed surface photometry has been made for six early-type barred spiral galaxies with use of high-resolution photographic plates. The main results obtained by detailed examination of several kinds of profiles are the following: (1) On the azimuthal luminosity profiles along the concentric ellipses, which should appear as circles centered on the nuclei in the planes of the galaxies, the bars appear as narrow humps superposed on the nearly flat axisymmetric components. The luminosity contrasts between the bars and the underlying axisymmetric components are quite large and have values ranging from 2.5–5.5. Fourier decompositions of these azimuthal profiles reveal that the largest contribution comes from the $m = 2$ component, but higher even-order components ($m = 4$, 6) are not negligible; a density distribution approximated by the $m = 2$ component alone is too simple to represent the observed bars. (2) The luminosity profiles along the bar major axes protrude prominently in the bar regions on the extrapolated straight lines of the outer exponential disks and have sharp cutoffs at the bar ends. The luminosity profiles along the bar minor axes have Freeman's type II shape. However, the azimuthally averaged radial luminosity profiles are Freeman's type I profile and are indistinguishable from those of ordinary spirals. (3) The bar components are extracted as nonaxisymmetric components with rectangular shapes by subtracting the underlying axisymmetric components from the original images. The luminosity distributions along the major axes of the extracted bars are expressed by exponential functions with shallow luminosity gradients and sharp cutoffs. The distributions perpendicular to the bars are described by Gaussian functions. (4) These observed properties of barred spirals are compared with the model bars formed in N-body simulations of a stellar disk. Significant differences in the luminosity distribution of the model bar have been found: (i) The gradient of the bar major axis profile is much steeper in the bar region than in the outer disk region, and there is no sharp cutoff at the bar ends. (ii) The azimuthal profiles in the bar region is well approximated only by the $m = 2$ and $m = 4$ components.

Subject headings: galaxies: photometry — galaxies: structure

I. INTRODUCTION

Barred spiral galaxies are one of the major categories of Hubble's (1926) classification scheme of galaxies and constitute about $\frac{1}{3}$ of all disk galaxies (de Vaucouleurs 1963*b*). Thus structure, evolution, and formation processes of barred spiral galaxies have been studied extensively. Ostriker and Peebles (1973) suggested that barred spiral galaxies could have been formed through so-called bar instability, if the stellar disks had been cold enough to be unstable for bar-type deformation. Lynden-Bell (1979) studied the trapping of stellar orbits by a barlike potential and proposed a mechanism for formation of stellar bars. Much progress has recently been made in theoretical studies of barred spiral galaxies, especially in numerical simulations. Various factors affecting bar formation processes have been studied, e.g., initial radial mass distributions by Hohl (1971, 1978) and Thielheim and Wolff (1984), vertical thicknesses of disks by Hohl (1978) and Combes and Sanders (1981), effects of spherical massive halos by Hohl (1976) and Sellwood (1980), and effects of nuclear bulges by Hohl (1978), Sellwood (1981, 1989), and Nishida (1986). These simulations have grown step by step to realistic models and have sometimes been compared with observed data of luminosity profiles by Baumgart (1983) and of kinematical properties such as mean streaming motions and velocity dispersions of stars by Kormendy (1983).

Interstellar matter in barred spiral galaxies has been studied as the dynamics of the gas rotating in the oval disk potential of the bars. Formation of both H II regions and dust lanes which are fairly commonly detected along the leading sides of the bars are believed to be the results of shock waves (Sørensen, Matsuda, and Fujimoto 1976; Sanders and Tubbs 1980; van Albada and Roberts 1981; Matsuda *et al.* 1987). Inner and outer rings of barred spiral galaxies may be related to the second harmonic resonances and outer Lindblad resonances, respectively (Schwarz 1981, 1984; Buta 1986*a*). Therefore, interstellar matter may play a large part in the structure and evolution of barred spiral galaxies. For a gasdynamics endurable for comparison with the observed kinematical properties of interstellar matters, oval gravitational potentials should be

[1] Guest Investigator at the Las Campanas Observatory, which is operated by the Carnegie Institution of Washington.
[2] Visiting Astronomer, Cerro Tololo Inter-American Observatory, National Optical Astronomy Observatories, operated by the Association of Universities for Research in Astronomy, Inc., under contract with the National Science Foundation.

TABLE 1

BASIC PARAMETERS OF PROGRAM GALAXIES

Object	Type[a]	Distance (Mpc)	Source[b]	B_T[a] (mag)	M_B (mag)	R_{25}[a] (arcsec, kpc)	PA[c]	E[d]	i[e]
NGC 1398.....	(R')SB(r)ab	18.7	1, 2	10.6	−20.8	198, 17.9	99°.8	0.26	43°
NGC 2217.....	(R)SB(rs)0$^+$	16.4	2, 3, 4	11.45	−19.6	144, 11.4	14.6	0.08	24
NGC 4440.....	SB(rs)a	25.1	2	12.75	−19.2	60, 7.3	40.0	0.36	52
NGC 4643.....	SB(rs)0/a	12.4	2, 4	11.55	−18.9	102, 6.1	61.0	0.15	33
NGC 4650.....	SB(s)0/a	36.4	5	12.8[f]	−20.0	135,[f] 23.8	160.8	0.18	36
NGC 4665.....	SB(s)0/a	15.3	4	11.43[g]	−19.5	125, 9.3	114.0	0.10	27

[a] From de Vaucouleurs, de Vaucouleurs, and Corwin 1976 (RC2).

[b] Sources of distances.—(1) Bottinelli *et al.* 1985; (2) Buta and de Vaucouleurs 1983; (3) Bottinelli *et al.* 1984; (4) Visvanathan and Griersmith 1979; (5) Palumbo, Tanzella-Nitti, and Vettolani 1983, from the recession velocity with $H_0 = 75$ km s^{-1} Mpc^{-1}.

[c] Position angle of the major axis of the galaxy (see text).

[d] Apparent ellipticity of the galaxy.

[e] $\cos^2 i = (q^2 - q_T^2)/(1 - q_T^2)$ (Hubble 1926), where q and q_T are apparent axial ratio $(1 - E)$ and intrinsic flattening of the disk, respectively, and q_T is given by $-\log q_T = 0.60 + 0.045T$, where T is Hubble sequence in RC2 numerical unit (Bottinelli *et al.* 1983).

[f] From ESO/Uppsala catalog (Lauberts 1982).

[g] Harvard photographic magnitude statistically corrected to the B_T system, m_c, from RC2.

modeled based on the observed luminosity distribution of stars as closely as possible. For this purpose and for comparison with the results of stellar dynamics of barred spiral galaxies, we urgently need to present luminosity distribution in detail with a high photometric accuracy and a high spatial resolution for stellar bar components which constitute the basic structure of barred spiral galaxies.

Since barred spiral galaxies are more complicated in their structure than ordinary spiral galaxies, surface photometry of barred spiral galaxies has not been well established except for examining the equivalent profiles or luminosity profiles along the major axes of bars or galaxies (de Vaucouleurs 1963*a*, *c*, 1975; Crane 1975; Benedict 1976; Baumgart 1983; Duval and Athanassoula 1983; Duval and Monnet 1985; Pence and de Vaucouleurs 1985). Recent developments in image processing as well as in instrumentation such as PDS microdensitometers and CCD detectors, however, enable us to examine the various kinds of luminosity profiles. For example, the azimuthal profiles, which are obtained along concentric circles centered on nuclei of galaxies, reveal that the bars appear as narrow humps superposed on the nearly flat component (Elmegreen and Elmegreen 1985, hereafter EE; Buta 1986*b*, 1987). Therefore, this technique is indispensable for surface photometry of barred spiral galaxies.

Since barred spiral galaxies sometimes show very sharp features around ridges and outer edges of the bars (Sandage 1961), plates taken with large telescopes are invaluable to achieve high spatial resolution, although data from low-resolution Schmidt plates are also important for a statistical study such as was done by EE. To disclose the framework of stellar components of barred spiral galaxies, surface photometry in *I* band may be suitable to record underlying old stellar populations effectively. However, it is much more important to select those early-type barred spiral galaxies which are devoid of H II regions and/or dust lanes. Taking account of these arguments, we made surface photometry in *B* band for six early-type barred spiral galaxies with distinct bars with the aid of the advanced image processing systems developed at the Kiso Observatory (Ichikawa *et al.* 1987) and at the Kyoto University. The results in this paper provide fundamental data for the studies of the structure, evolution, and formation of barred spiral galaxies. The names of the program galaxies and their basic parameters are listed in Table 1.

In § II, observations and data reductions are given, and in § III azimuthal luminosity profiles are extracted and analyzed extensively. Radial luminosity profiles of the bars and underlying disk components are studied in § IV. In § V, the bar components are properly extracted by subtracting the axisymmetric components from the original images, and then the structure of the extracted bars is studied extensively. Finally, in § VI, the observed properties are compared with the results of numerical simulations of a stellar disk.

II. OBSERVATIONS AND DATA REDUCTION

Photographic plates of the program galaxies were taken with the 2.5 m du Pont and 1 m Swope telescopes at the Las Campanas Observatory and with the 4 m telescope at the Cerro Tololo Inter-American Observatory. All the plates were taken in *B* band, except for the plates of NGC 4650, which were taken with IIIa-J emulsion behind a GG385 filter. Seeing sizes were typically about 2″ (FWHM) for most of the plates. A journal of the plates is given in Table 2, and the photographs of the program galaxies are reproduced in Figure 1 (Plate 1).

The plates were measured with the PDS microdensitometers at either the National Astronomical Observatory or the Kiso Observatory with scanning parameters given in Table 3. The scanned areas on the plates were taken to be about 3 times as large as D_{25}, the diameters of the galaxies given in the *Second*

TABLE 2

PHOTOGRAPHIC PLATE MATERIAL

Object	Plate Number[a]	Emulsion[b]	Filter	Exposure (minutes)
NGC 1398.....	CD839	103a-O	Wr2C	30
	CD848	103a-O	Wr2C	6
NGC 2217.....	CF2170	IIa-O	GG385	105
	CF2206	IIa-O	GG385	12
NGC 4440.....	CD845	103a-O	Wr2C	75
NGC 4643.....	CD852	103a-O	Wr2C	75
NGC 4650.....	CTIO6291	IIIa-J	GG385	5
	CTIO6292	IIIa-J	GG385	50
NGC 4665.....	CD852	103a-O	Wr2C	75

[a] The prefixes CD, CF, and CTIO stand for the plates taken with the 2.5 m du Pont, 1.0 m Swope, and CTIO 4 m telescopes, respectively, with the plate scales, 10.9, 29.0, and 18.6 arcsec mm^{-1}.

[b] All emulsions were hypersensitized.

PLATE 1

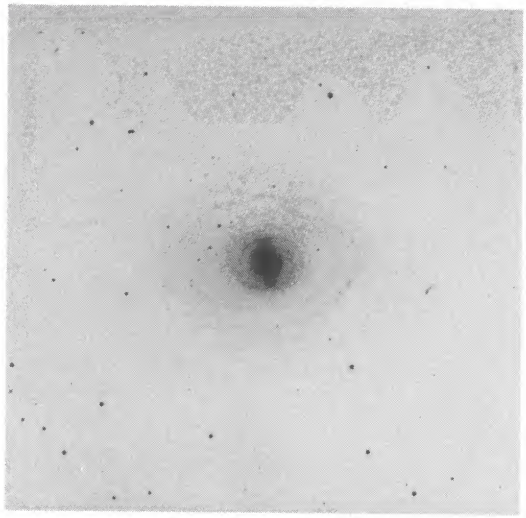

NGC 1398

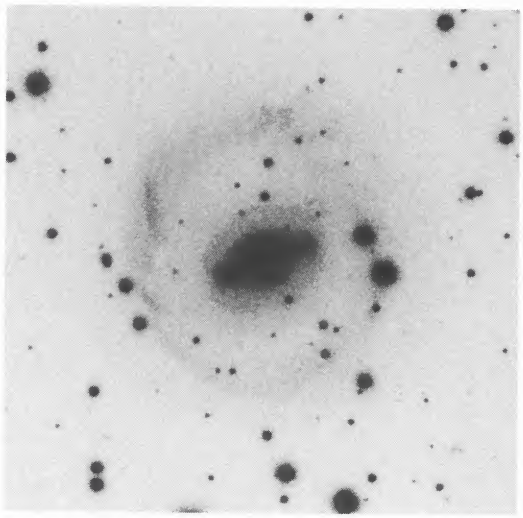

NGC 2217

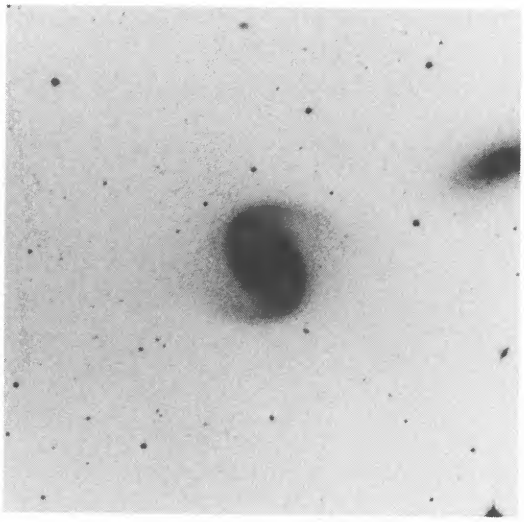

NGC 4440

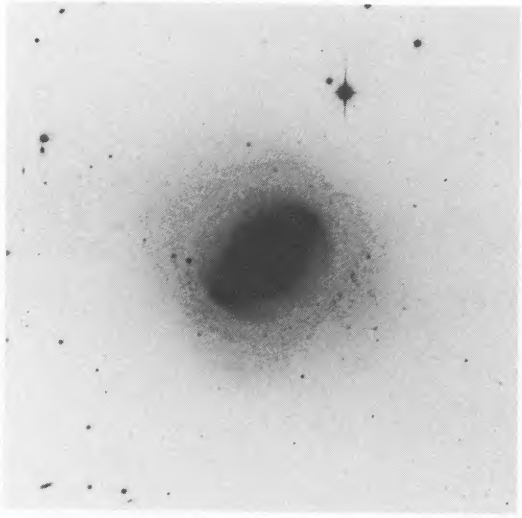

NGC 4643

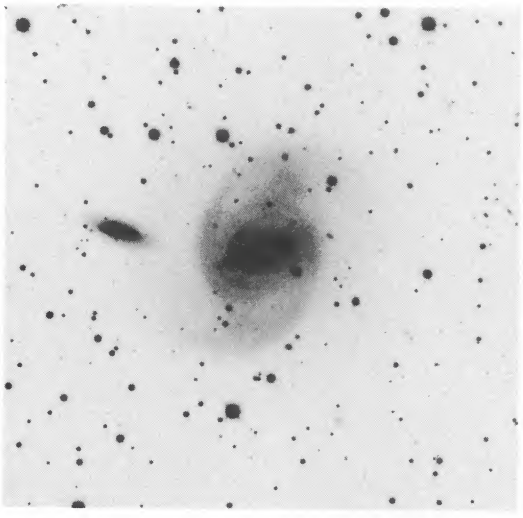

NGC 4650

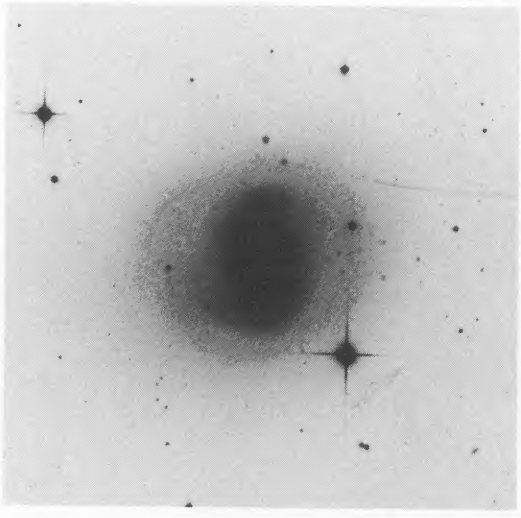

NGC 4665

FIG. 1.—Photographs reproduced from the original plates. North is at the top and east is at the left. The sizes of the frames are 800″ for NGC 1398 and 400″ for the other 5 galaxies. The journal of the plates is given in Table 2.

TABLE 3

SCANNING PARAMETERS OF PLATES AND THE SKY BRIGHTNESS

Object	Aperture (μm)	Pitch (μm)	Pixel Size (arcsec pixel^{-1})	Sky Brightness (mag arcsec^{-2})
NGC 1398.....	100	92	2.01[a]	21.66 ± 0.24
NGC 2217.....	42	34	1.00	22.11 ± 0.02
NGC 4440.....	42	46	1.00[a]	22.13 ± 0.09
NGC 4643.....	95	92	1.00	22.47 ± 0.08
NGC 4650.....	50	50	0.93	22.00[b]
NGC 4665.....	95	92	1.00	22.47 ± 0.06

[a] Final image was obtained through binning of 2 × 2 pixels in the original image.

[b] Assumed owing to lack of photoelectric aperture photometry.

Reference Catalogue of Bright Galaxies (de Vaucouleurs, de Vaucouleurs, and Corwin 1976, hereafter RC2), and hence they were large enough for reliable sky background subtractions.

Data reductions were carried out with the image processing software library "SPIRAL" at the Kiso Observatory (Ichikawa *et al.* 1987; Okamura 1988). The outline of the procedures is as follows. A density image was transformed into an intensity image through a characteristic curve which was approximated with a Goad function. A sky background was determined by fitting a two-dimensional polynomial of the first or third (the fifth for NGC 4440) order to the data points in the sky region. By interpolating it into the object region, the sky background was subtracted from the original intensity image with the precision of about 2% of the sky level. The resultant image was divided by the sky background image for normalization, and thus the relative intensity image was obtained for each galaxy. To increase the signal-to-noise ratio, smoothing with a variable-width Gaussian beam was applied to the fainter region of the galaxy. For the objects for which two plates are available, two sets of the image data were composed into one image by weighting a short- or long-exposure plate for a bright or faint region of the galaxies, respectively. Foreground stars and plate defects were removed if necessary. It is noted that a bright star within the isophote of 26 mag arcsec^{-2} in NGC 4665 was replaced with the pixels located symmetrically with respect to the nucleus of the galaxy. Magnitude calibrations were made by comparing the present data with multiaperture photoelectric photometry (Longo and de Vaucouleurs 1983), and the resulting sky brightness for each galaxy is given in Table 3. The isophotal maps before removal of stars are shown in Figure 2.

Since no published data of surface photometry in *B* band are available for the program galaxies, the accuracy of the present analysis was checked by similarly reducing the E0 galaxy NGC 4636 which is exposed on the same plate as NGC 4643 and NGC 4665. The luminosity profile of NGC 4636 was compared with that obtained by King (1978). Overall shapes of the profiles agree with each other within ±0.1 mag arcsec^{-2} in the range $\mu_B \sim$ 18–26 mag arcsec^{-2}. However, the zero point of our magnitude scale was found to be 0.65 mag arcsec^{-2} brighter than that of the King data. A similar disagreement was also noticed by Ichikawa (1987), and it may be an error in the King data.

III. AZIMUTHAL PROFILES

a) *Extraction of Azimuthal Profiles*

For a quantitative study of the barred structure, we examine luminosity profiles extracted along concentric ellipses which should appear as circles centered on the nuclei in the planes of the galaxies. The ellipticity and position angle of the major axis of the ellipse, and therefore the inclination of each galaxy, are determined by fitting an ellipse to the outermost isophote (μ_B = 25.0 or 26.0 mag arcsec^{-2}), and they are tabulated in Table 1.[3] Inclinations were calculated on the assumption that faint outer regions of barred spirals are in circular symmetry without influence of the presence of bars. This is justified by the fact that, as shown in Figure 2, the contours fainter than μ_B = 25 mag arcsec^{-2} lie far outside the bar region in each galaxy and are well-fitted to ellipses with almost the same ellipticity and position angle of the major axis, except for NGC 4440 and NGC 4650, both of which have close companions. The circular symmetry of the outer regions is also verified from a statistical study of axial ratios of 160 barred spiral galaxies (see Appendix).

Along these similar ellipses with various sizes, luminosity profiles are obtained, at a spacing of 1° in azimuthal angle, with a box-shaped aperture (4″ × 2″) which has a Gaussian weight with a standard deviation of 2″. They are shown in Figure 3 as a function of inclination-corrected azimuthal angle θ and are referred to hereafter as azimuthal profiles.

The azimuthal profiles vary with radius in both amplitude and shape. The profiles are nearly flat in the inner regions where nuclear bulges dominate. As the radius increases, prominent humps corresponding to the bars appear with the period of 180°. After reaching their peak values at intermediate radii inside bars, the amplitudes of the profiles decrease outward. Beyond the sharp ends of the bars, the profiles get flat again for the galaxies with no or little arms (e.g., NGC 4643 and NGC 4665), while for the galaxies with prominent arms (e.g., NGC 4440 and NGC 4650), they remain wavy, and the azimuthal angles of the peaks vary with radius.

b) *Fourier Decomposition*

The present program objects are early-type galaxies and hence lack either prominent dust lanes or chains of H II regions which are frequently observed along the bars in intermediate- or late-type barred spiral galaxies. Thus they are appropriate to analyze the structure of stellar bars. In the works of EE and Buta (1986*b*, 1987), the azimuthal profiles $I(r, \theta)$ are analyzed with Fourier decomposition:

$$I(r, \theta) = A_0(r)/2 + \sum [A_m(r) \cos m\theta + B_m(r) \sin m\theta] ,$$

where

$$A_m(r) = 1/\pi \int_0^{2\pi} I(r, \theta) \cos m\theta \, d\theta ,$$

and

$$B_m(r) = 1/\pi \int_0^{2\pi} I(r, \theta) \sin m\theta \, d\theta .$$

[3] The position angle of NGC 4440, 81°.5, derived on the present scheme yields not a straight but a skewed extracted bar (§ V*a*), though the bar is straight on the photograph (Fig. 1). After trial and error, we adopted the position angle of the major axis so that the bar can be extracted as a straight component. (Ellipticity is not sensitive for the extraction of a straight bar.) The above error in the position angle may be caused by either distortion of outer disk due to possible tidal interaction with the neighboring galaxy NGC 4436 (V = 1163 km s^{-1}; Binggeli, Sandage, and Tammann 1985) or inaccurate sky subtraction due to its location close to the plate edge.

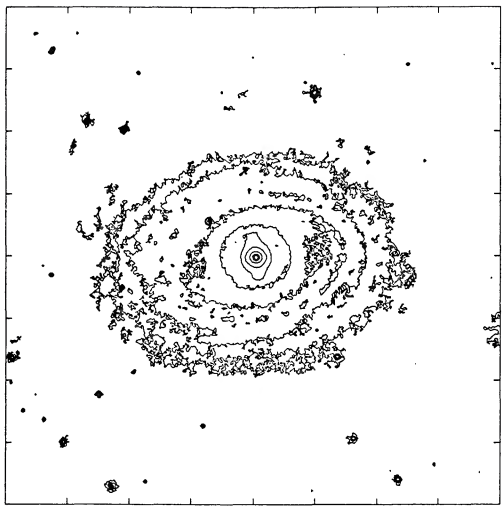

NGC 1398

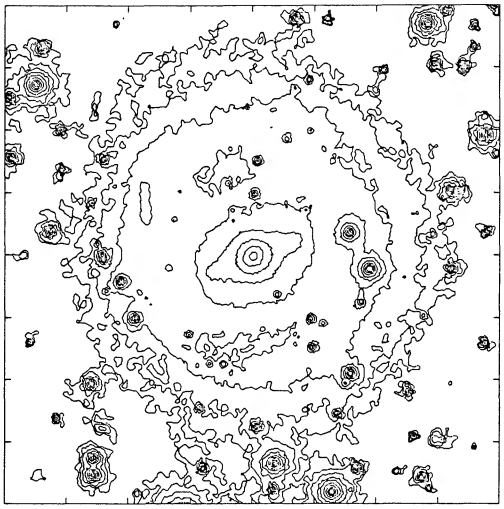

NGC 2217

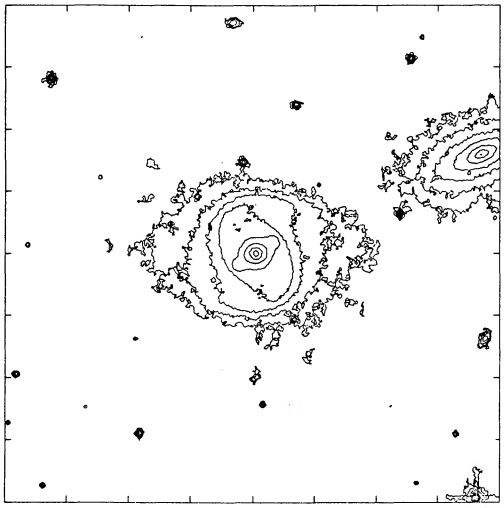

NGC 4440

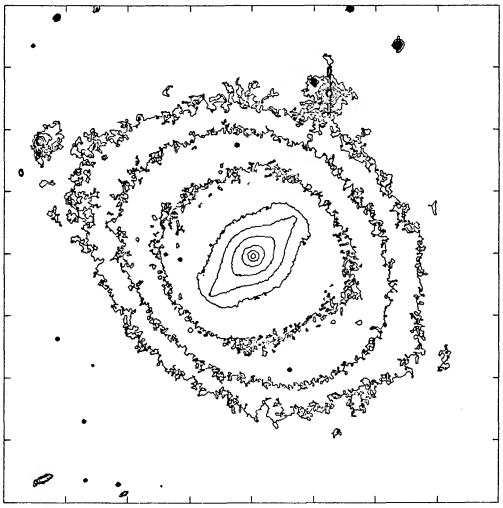

NGC 4643

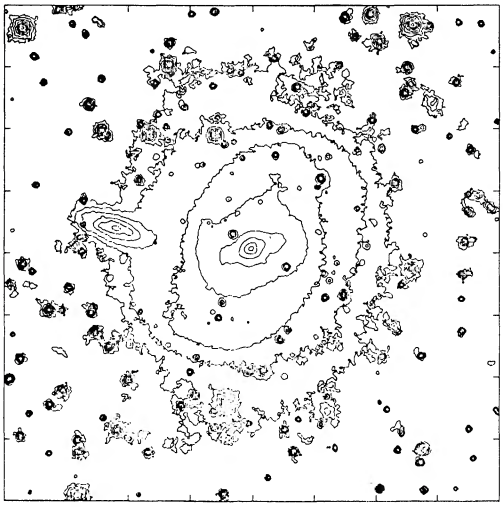

NGC 4650

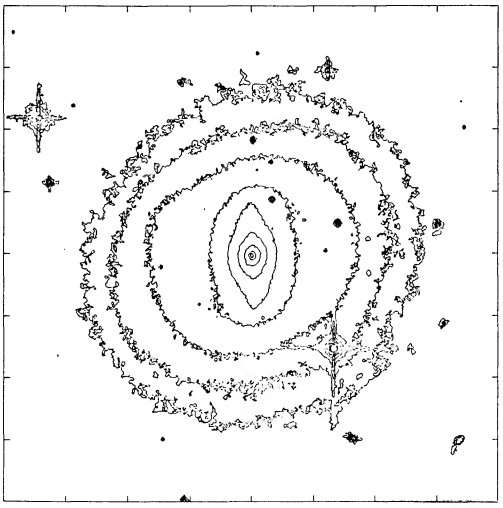

NGC 4665

FIG. 2.—Isophotal maps of program galaxies before removal of stars. North is at the top and east is at the left. The outermost isophotes correspond to 26 mag arcsec^{-2}, and isophote interval is 1 mag arcsec^{-2}. Areas of isophotes are the same as those in Fig. 1, and the interval of tick marks on the borders is 100″ for NGC 1398 and 50″ for the other five galaxies.

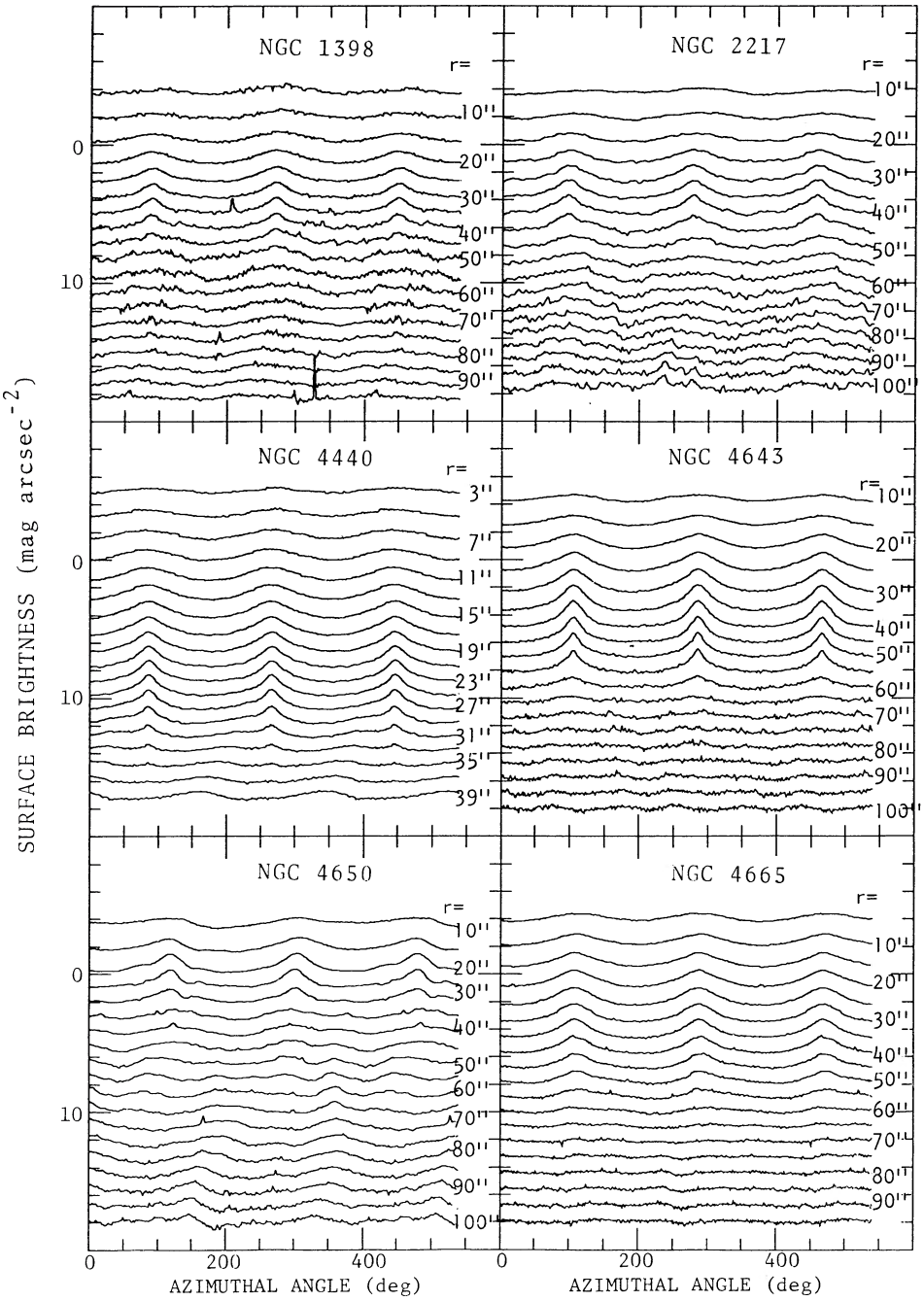

FIG. 3.—Azimuthal profiles traced along the concentric circles centered on the nucleus of the galaxy in the plane of the galaxy. The ordinate represents surface brightness (mag arcsec^{-2}) with arbitrary zero point. The abscissa is the inclination-corrected azimuthal angle with an arbitrary zero point. A total of 1.5 cycles are shown. The inclination-corrected radius for each profile is given at the right end of the profile.

Fourier amplitude of the mth component is defined as

$$I_0(r) = A_0(r)/2 ,$$

$$I_m(r) = [A_m(r)^2 + B_m(r)^2]^{1/2} .$$

The relative amplitudes $[I_m(r)/I_0(r)]$ of the first eight components are shown in Figure 4 as a function of radius. A horizontal line in each panel shows a bar region defined in § III*d*.

Throughout the bar region, the relative amplitudes of even components are much larger than those of odd components. The most dominant even component is, of course, $m = 2$, and the amplitudes decrease steadily at any radius, as far as the higher even-order components are concerned. The peak amplitudes reach about 0.5, 0.25, 0.15, and 0.1 for the $m = 2$, 4, 6, and 8 components, respectively.

c) Representation of Bar Component with Fourier Components

As seen typically in NGC 4643, the azimuthal profiles in the bar regions look like a superposition of narrow humps on nearly flat components rather than like a pure sinusoidal curve. The deviation from a sinusoidal curve is represented by

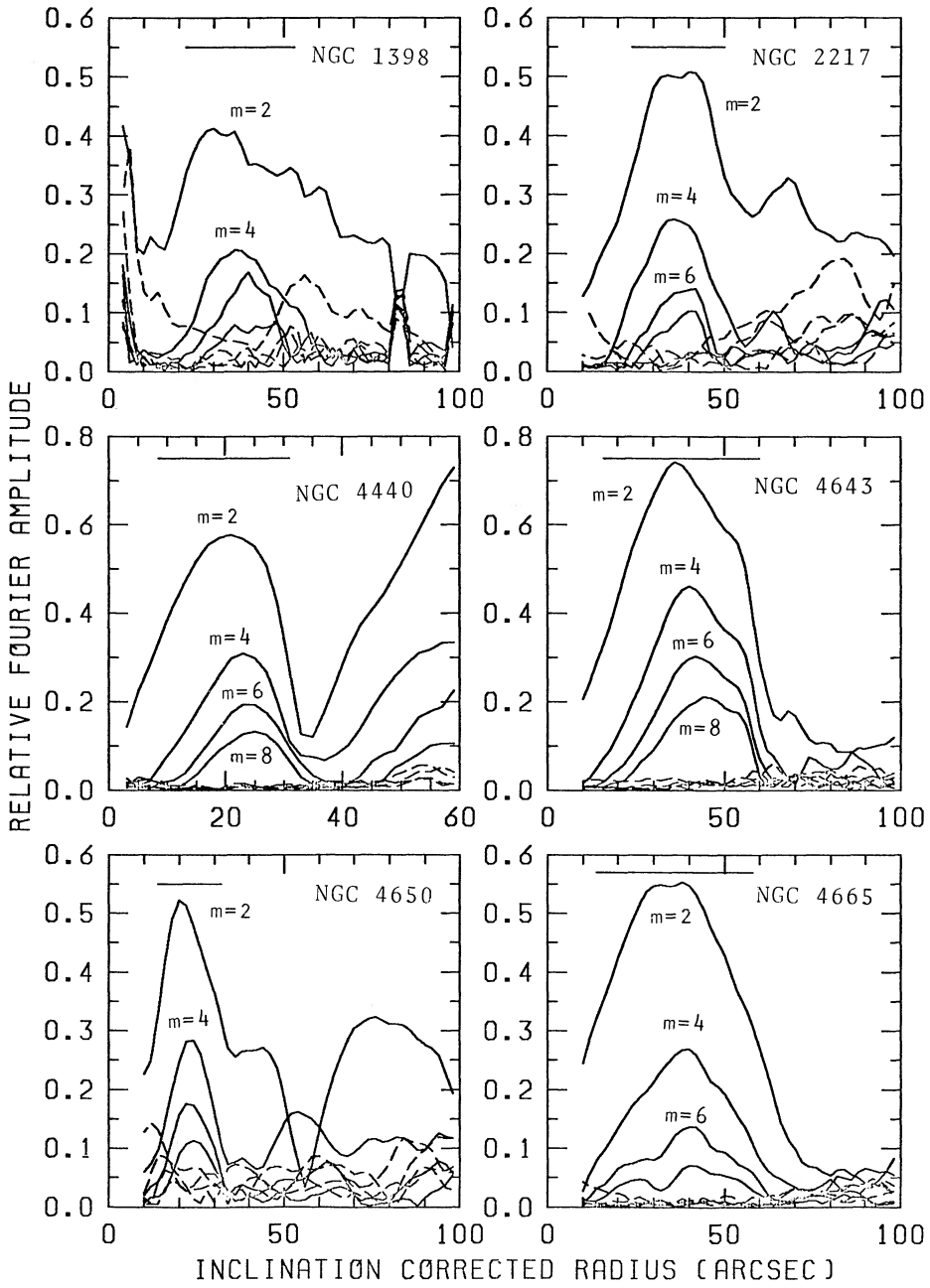

FIG. 4.—Relative amplitudes of Fourier components (I_m/I_0; $m = 1, \ldots, 8$) are given as a function of inclination-corrected radius. Solid lines and dashed lines show even and odd components, respectively. Horizontal lines indicate the bar regions defined in § III*d*.

the amount of contribution from the higher even-order components relative to the $m = 2$ component, i.e., I_m/I_2 ($m = 4, 6, 8, \ldots$). The ratios I_4/I_2, I_6/I_2, and I_8/I_2 become larger as the hump gets narrower. For the present program galaxies, the ratios I_4/I_2 and I_6/I_2 amount to about 0.5 and 0.3, respectively. Large $m = 4$ and 6 amplitudes were also found for the bar region of NGC 1433 (Buta 1986*b*), and higher order terms up to $m = 10$ would probably have been significant. Hence, a density distribution approximated by only the $m = 2$ component is too simple to represent the observed bars and may cause a serious error in theoretical studies of the dynamics of barred spiral galaxies (see also Petrou 1984). At least the $m = 4$ component should be included for detailed numerical simulations.

As shown in Figure 4, the peak radius of each curve shifts outward as the higher even-order components are concerned. This trend is only due to a geometric effect. Since the widths of bars are constant along their major axes (see § III*d*), the angles of the bars subtended by the nuclei decrease outward and therefore increase the contribution of the higher even-order components.

Even beyond the ends of the bars, the contribution from the $m = 2$ component is significantly larger than noise level (Fig. 4). This is caused by the bisymmetric structure of the arms (e.g.,

NGC 4650; see also Buta 1986*b* for the case of NGC 1433) or the ring (e.g., NGC 2217). However, even for the galaxies without remarkable arms or rings, e.g., NGC 4643 and NGC 4665, the $m = 2$ component remains clearly above the noise level up to the radius of about 2 times the bar radius, r_{bar}, which is defined in § III*d*. This may represent the distortion of the outer disk by the presence of the bar.

d) *Luminosity Contrast between the Bar and the Interbar*

The azimuthal profiles around the peaks are broad enough to be resolved spatially on our high-resolution plates, and so the peak amplitudes of the bars are not blurred due to the seeing effect. The luminosity contrasts between the bars and the interbars, I_b/I_{ib}, are shown in Figure 5 in solid lines as a function of the radius, where I_b and I_{ib} are the intensities at the peak and at the bottom of an azimuthal profile, respectively. In order to avoid noise fluctuations on the profiles, we adopt $(I_0 + I_2 + I_4 + I_6)$ and $(I_0 - I_2 + I_4 - I_6)$ as I_b and I_{ib}, respectively. The resultant contrasts are also drawn in Figure 5 in dashed lines. Because of exclusion of the remaining higher order Fourier components, they are smaller at any radius than those drawn in solid lines, although the overall shapes of the curves are essentially the same. The contrast is low in the inner region where the nuclear bulge dominates. Beyond the bulge region, it increases steeply and attains its peak value in the middle radius of the bar and falls steeply toward the bar end. The maximum contrasts measured in the dashed lines are surprisingly large: they amount to ~5.5 for NGC 4643, ~3.8 for

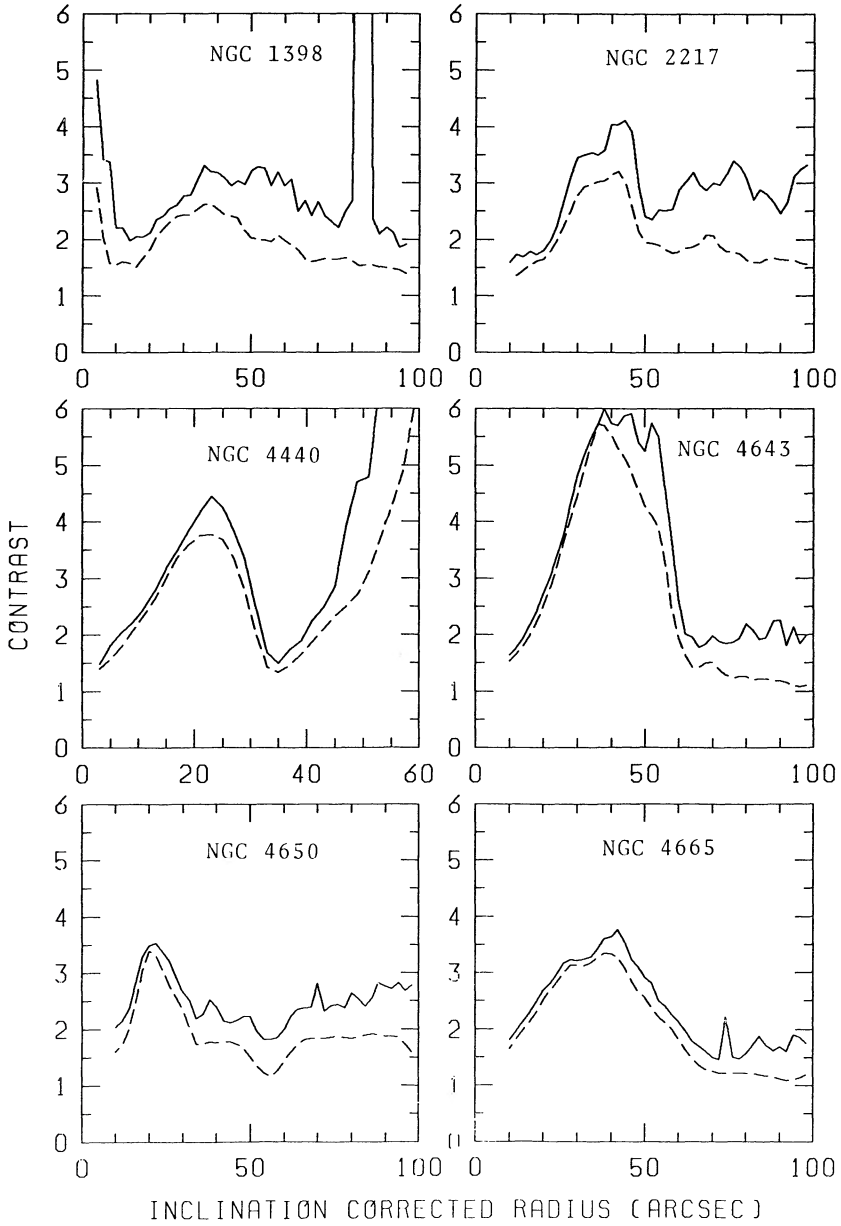

FIG. 5.—Luminosity contrasts between the bars and interbars as a function of inclination-corrected radius. Solid lines show the ratio of the peak intensity to the bottom intensity of the azimuthal profiles. Dashed lines show the ratio of $(I_0 + I_2 + I_4 + I_6)$ to $(I_0 - I_2 + I_4 - I_6)$, where I_m denotes a Fourier amplitude of mth component. See the text for the details. A spike in the solid line at $r = 85''$ for NGC 1398 is caused by the presence of an H II region.

TABLE 4

PARAMETERS OF BARS

Object	r_{bulge} (arcsec, kpc)	r_{bar} (arcsec, kpc)	w_{bar} (arcsec, kpc)	$\frac{w_{bar}}{r_{bar}}$	$\frac{r_{bar}}{r_0}$[a]	$f_{bar}(r_{bulge} < r < r_{bar})$[b]	$f_{bar}(r < R_{25})$[b]
NGC 1398.....	22, 2.0	53, 4.8	18, 1.6	0.34	0.9	0.27	0.26
NGC 2217.....	24, 1.9	50, 4.0	17, 1.4	0.34	...	0.31	0.12
NGC 4440.....	8.5, 1.0	31, 3.8	8.3, 1.0	0.27	1.7	0.35	0.17
NGC 4643.....	16, 1.0	60, 3.6	11, 0.7	0.18	1.8	0.43	0.30
NGC 4650.....	14, 2.5	32, 5.6	8.3, 1.5	0.26	0.9	0.30	0.11
NGC 4665.....	14, 1.0	58, 4.3	18, 1.3	0.31	1.8	0.48	0.31

[a] The values of r_0, the scale length of the exponential disk, are given in Table 5.
[b] Luminosity fraction of bar (see text).

NGC 4440, ~3.2 for NGC 2217, NGC 4650, and NGC 4665, and ~2.5 for NGC 1398. The bars with such high contrasts can distort the disk potential so significantly from a circular symmetry that they may not be treated as perturbations in dynamical studies.

We define a bar region as the zone where the contrast exceeds 2.0 on the dashed lines in Figure 5. Their inner and outer edges are determined unambiguously. At the inner edge, the contribution from the bar light is comparable to that from the bulge (contribution from the disk light is typically ~20%), and so we call this the bulge-dominated radius, r_{bulge}. The outer edge is called the bar radius, r_{bar}. These radii are listed in Table 4 for each galaxy.

From the angular widths ($\frac{1}{2}$ FWHM in arcseconds) of the humps on the azimuthal profiles, we calculate inclination-corrected linear widths of the bars, w_{bar}, at various radii. The widths change less than 10% along the major axis of the bar in each galaxy. Therefore, the bar is not like a sector structure but rather like a bar structure with a nearly constant width along its major axis. In Table 4, we list the averaged bar width w_{bar} and the axial ratio of the bar defined as w_{bar}/r_{bar}.

e) Symmetry with Respect to the Nucleus

The azimuthal profile $I(r, \theta)$ is expressed as

$$I(r,\theta) = \frac{I(r,\theta) + I(r,\theta + 180°)}{2} + \frac{I(r,\theta) - I(r,\theta + 180°)}{2},$$

where the first and second terms represent the symmetric and antisymmetric parts with respect to the nucleus, respectively. Since the sine and cosine functions have the properties of $f[m(\theta + 180°)] = (-1)^m f(m\theta)$, the above symmetric or antisymmetric terms are expressed with even or odd Fourier components, respectively. The dominance of even Fourier components over odd components shown in Figure 4 represents a high degree of symmetry of the bar with respect to the nucleus. The relative amplitude of each odd component contributes at most 5% for the galaxies with high symmetry, e.g., NGC 2217, NGC 4440, NGC 4643, and NGC 4665, and less than 10% for the other two galaxies. Note that the odd components are not negligible outside the bar ends of NGC 1398 and NGC 2217. These may be caused by the presence of spiral arms (NGC 1398) or an outer ring (NGC 2217).

f) Straightness of Bar

In Figure 6, we plotted the azimuthal angles of the peaks of the humps on the azimuthal profiles in the bar regions as a function of radius together with the angular separations between the two peaks. These angles are determined by fitting a Gaussian to the peak region ($\pm 10°$) of the azimuthal profiles so as to avoid the influence of noise fluctuation. As shown in Figure 6, the peaks lie at a constant angle within about $\pm 2°$ along the radius, and their angular separations are $180° \pm 2°$ (1 σ), for all the objects except NGC 4650. Note that the ambiguity of 2° in azimuthal angle corresponds to 1″–2″ or 1–2 pixels for the bar regions. Hence, the ridges of the bars in these galaxies are found to show no deviation from a straight line larger than the present detection limit of $\pm 2°$.

g) Symmetry with Respect to the Bar Major Axis

In order to detect any systematic asymmetry in luminosity distribution between the leading and trailing sides of the bars, the azimuthal profiles $I(r, \theta)$ are expressed as

$$I(r,\theta) = \frac{I(r,\theta) + I(r,2\phi - \theta)}{2} + \frac{I(r,\theta) - I(r,2\phi - \theta)}{2}, \quad (1)$$

where the first and second terms represent a symmetric and antisymmetric part, respectively, with respect to the position angle of the major axis of the bar ϕ. The angle ϕ is determined, with the precision of 0°.5 for each bar, so as to minimize the contribution from an antisymmetric part. Note that even a small error in ϕ causes a sharp dip-and-spike profile (like the spectrum of a P Cygni–type star) around narrow peaks with steep gradient. In Figure 7 we show four kinds of profiles across the northern bar of NGC 4643 at four bar-dominated radii: the original $I(r, \theta)$, the symmetric part, the antisymmetric part, and the ratio of the intensities of the antisymmetric to symmetric part. The profiles of the antisymmetric part show no systematic trends across the bar amounting larger than 5% of the symmetric part. Similar conclusions are also obtained for the other objects. Thus, the systematic differences in the luminosity distributions between the leading and trailing sides of the bars are less than 5%–10%, indicating the highly symmetric structure of the bar with respect to its major axis. CCD observations are required for finer measurement.

IV. RADIAL PROFILES

In order to study the radial structures of bars, disks, and bulges further, we construct luminosity profiles along the major and minor axes of the bars, as well as the azimuthally averaged profiles, i.e., the profiles averaged over 360° along the ellipses introduced in § III*a*. The profiles were constructed in the deprojected galaxy images. To improve the signal-to-noise ratio, the major and minor axis profiles were averaged over azimuthal angles and folded with respect to the center of the galaxy. The adopted angular widths for averaging are taken to be large enough to improve the signal-to-noise ratio but small enough not to smooth out the profiles, and thus they depend

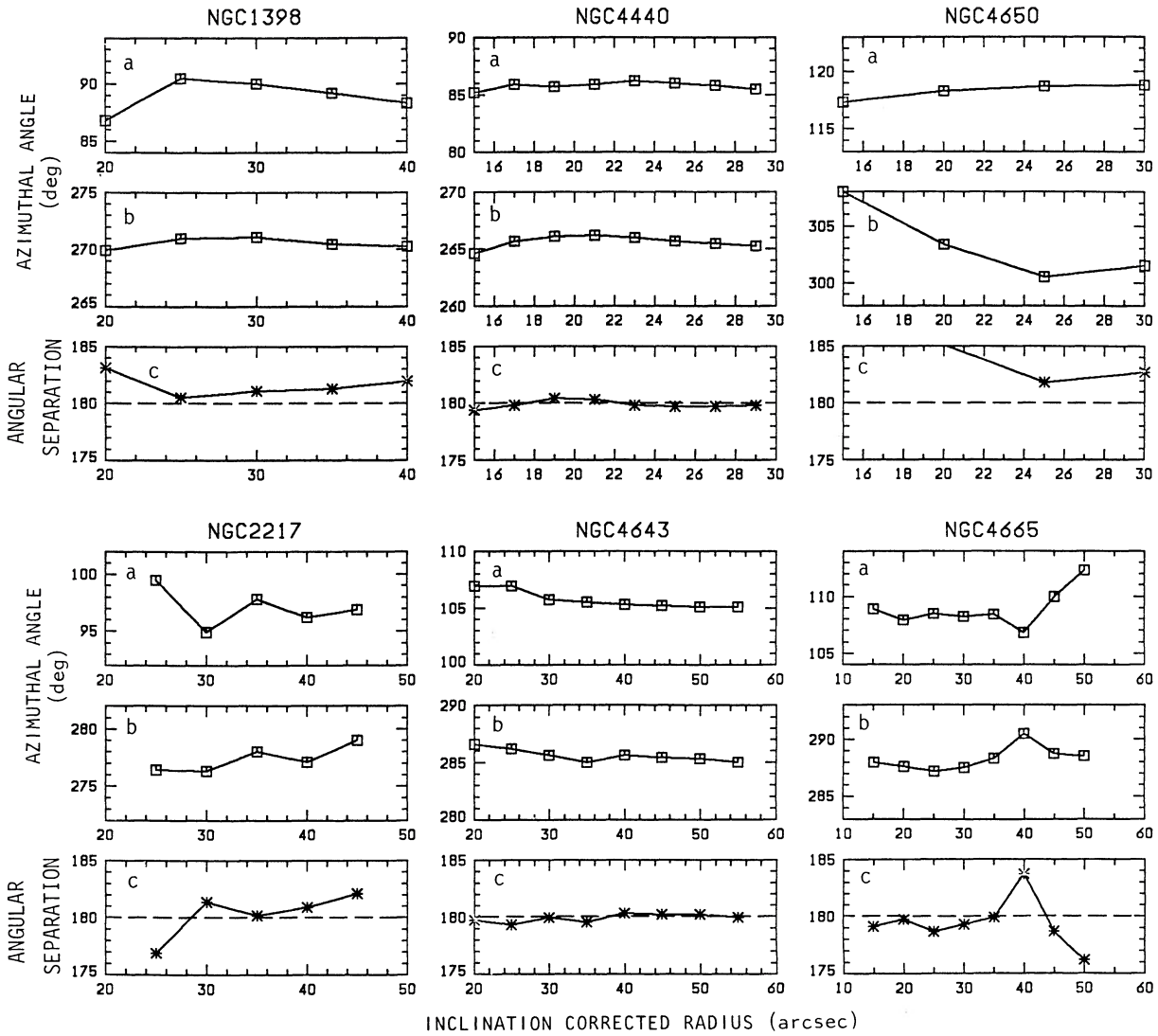

FIG. 6.—Straightness of the bar components. (*a*), (*b*) Azimuthal angles of the two peaks on the azimuthal profiles are given as a function of the inclination corrected radius. (*c*) Angular separations of the two peaks are given as a function of the inclination-corrected radius.

on the angular widths of both humps and flat parts on the azimuthal profiles. For the bar major axis profiles, we adopted 20° for all the galaxies, while for the bar minor axis profiles we took 36° for NGC 1398, 60° for NGC 2217, 45° for NGC 4440, NGC 4643 and NGC 4665, and 30° for NGC 4650. Note that the bar minor axis profiles are contaminated by the bar light in the central region $r < w_{\rm bar}$. These three kinds of radial profiles are shown in Figure 8.

Each profile consists of three regions: a nuclear bulge region, a bar region, and an outer disk region. The bar region defined in § III*d* is indicated by a horizontal line. On the bar major axis profiles, the bars are found to have very sharp outer edges at the bar ends. The *e*-folding linear scales at these edges are 1400 pc (NGC 1398), 780 pc (NGC 2217), 710 pc (NGC 4440), 420 pc (NGC 4643), 1700 pc (NGC 4650), and 1500 pc (NGC 4665). Outside the bar region, the three profiles, except for those of NGC 4440, join each other up to the radius where the surface brightness decreases to $\sim 1/100$ of the sky brightness. Beyond this level, they do not agree well with each other any more, probably due to errors in sky subtraction. The close agreement of the three profiles in the outer region simply implies that the isophotes in the outer disk region are well fitted to ellipses with the same ellipticity and position angle of the major axis, and thus this supports the assumption of a circular symmetry of the outer disk.[4] As shown in Figure 8, the profiles in the outer disk regions can be fitted to straight lines, i.e., an exponential law. Even for NGC 4440, the azimuthally averaged profile fits well to the exponential law, though the bar major and minor axis profiles deviate significantly each other. For NGC 2217, which has a prominent outer ring, its three profiles agree with each other and also fit to the exponential law outside the ring.

In the bar regions, the bar minor axis profiles have shallower luminosity gradients than those of outer exponential disks. This makes the bar minor axis profiles look like Freeman's (1970) type II profiles. On the bar major axis profiles, the bars appear as luminous humps of about 1 mag excess in surface brightness over the bar minor axis profiles and protrude prominently from the straight lines extrapolated from the outer exponential disks. However, the azimuthally averaged

[4] This is not the case in NGC 4440. The cause of this is mentioned in the footnote in § III*a*.

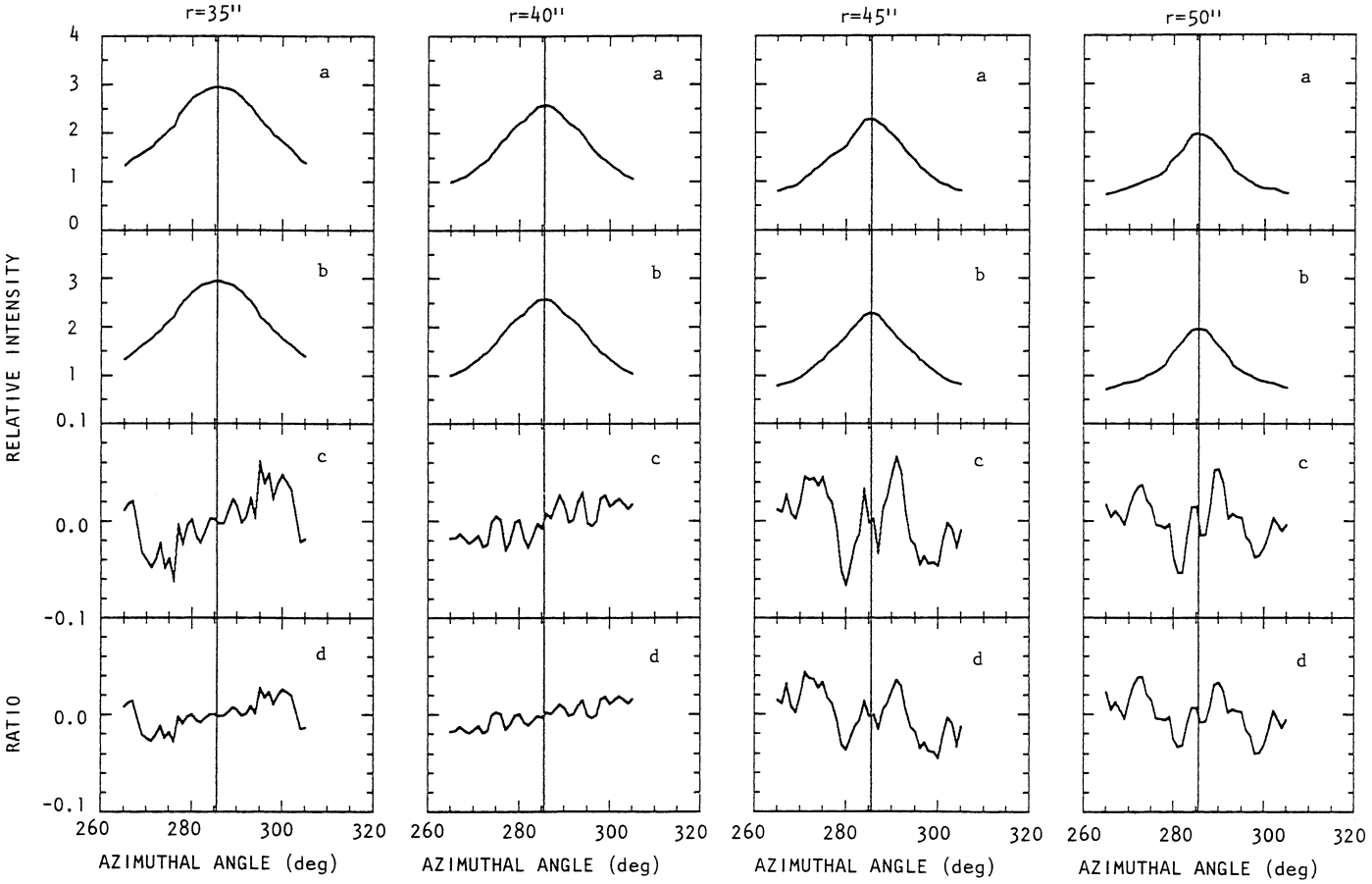

FIG. 7.—Symmetry of the luminosity profiles between the leading and trailing sides of the northern bar of NGC 4643. In (*a*), the observed azimuthal profiles around the ridges of the northern bar are given at four bar-dominated radii. With use of eq. (1), they are decomposed into the symmetric part (panel [b]) and the antisymmetric part (panel [c]). (*d*) shows the intensity ratio of the antisymmetric part to the symmetric part. Ordinates of the panels (*a*), (*b*), (*c*) are represented in intensity scale. Vertical lines show the symmetric axes of the profiles.

profiles, which run, of course, between the bar major and minor axis profiles in the bar regions, merge into the outer exponential disks smoothly and continuously, without any luminosity jumps[5] at the bar ends. That is, the luminosity excesses of the bar components on the bar major axis profiles are canceled by the dips on the minor axis profiles. Therefore, the azimuthally averaged profiles show no traces of the presence of the bars and have the shape of Freeman's (1970) type I profile. The barred spiral galaxies, which are characterized by the presence of prominent nonaxisymmetric bar components, are found to have azimuthally averaged radial luminosity profiles similar to those of ordinary spiral galaxies. Similar results were obtained by EE from the azimuthally averaged *I* band luminosity profiles. Among their 15 barred spiral galaxies studied, only NGC 1300 shows a hint of type II profile, while the others have type I profiles.

We decomposed the azimuthally averaged profiles into an exponential disk and an $r^{1/4}$-law bulge iteratively. The resultant decompositions are reasonable at all radii except for the central regions within 3″–4″, where surface brightness of decomposed bulges exceed those of observations. The obtained parameters are the scale length, r_0, and the central surface brightness, $B(0)_c$, for the exponential disk, and the half-luminosity radius, r_e, and the surface brightness at r_e, μ_e, for the $r^{1/4}$-law bulge. We also derived bulge-to-disk luminosity ratios using these parameters. The resultant parameters are listed in Table 5. There is no clear trend that these parameters are systematically larger or smaller than those of ordinary spiral galaxies derived by Burstein (1979), Boroson (1981), and Kent (1985). Hence, barred spiral galaxies are indistinguishable from ordinary spiral galaxies with respect to these parameters alone. Similar results are obtained from a statistical study of the azimuthally averaged luminosity distribution of 119 ordinary and barred spiral galaxies (Kodaira, Watanabe, and Okamura 1986).

These results may imply the following: if bars could have been formed from disks of an azimuthally averaged radial mass distribution similar to Freeman's type I disk, such as might have been the case for ordinary spiral galaxies, azimuthal redistribution of matter should have occurred during bar formation without net radial redistribution of matter. On the other hand, if they could have been formed from disks of an azimuthally averaged radial mass distribution deviating significantly from Freeman's type I disk, an efficient mechanism should have operated, during or after the formation of bars, to

[5] NGC 1398 has a small but clear luminosity excess up to the radius $r = 55''$ even on the bar minor axis profile. This is caused by the presence of a prominent lens system surrounding the whole bar region and partly due to an inner pseudoring (see also Fig. 1). Ringed barred spiral galaxies, e.g., NGC 1433 (Buta 1986*b*), may have more complicated structure than those of nonringed barred spiral galaxies.

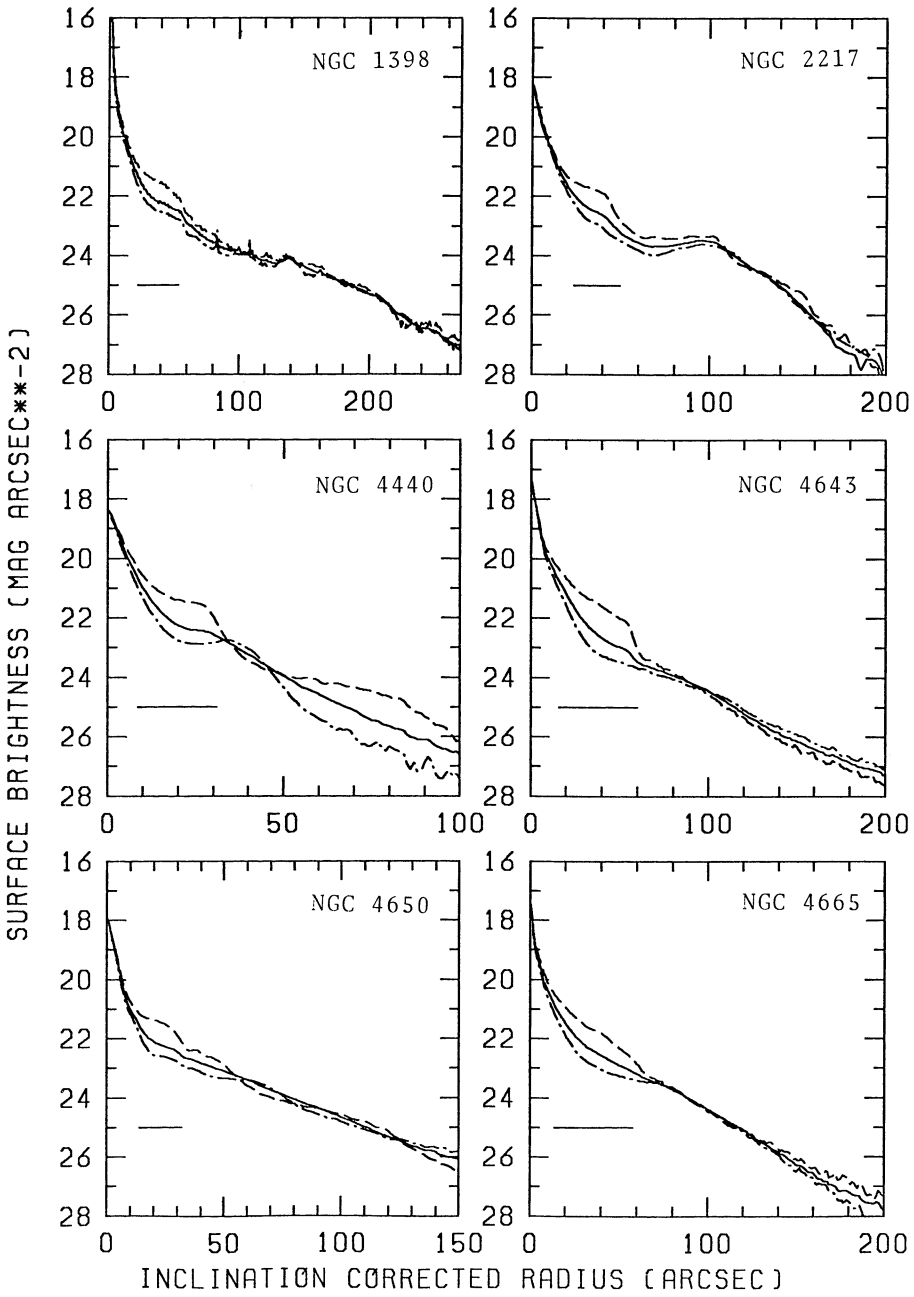

FIG. 8.—The radial luminosity profiles along the bar major axis (*dashed lines*) and bar minor axis (*dash-dotted lines*), and the azimuthally averaged (*solid lines*) profiles are given against the inclination-corrected radius. Horizontal lines indicate the bar regions defined in § III*d*.

TABLE 5

PARAMETERS FOR THE OUTER DISKS AND THE BULGES[a]

OBJECT	DISK		BULGE		BULGE-TO-DISK RATIO
	$B(0)_c$ (mag arcsec^{-2})	r_0 (arcsec, kpc)	μ_e (mag arcsec^{-2})	r_e (arcsec, kpc)	
NGC 1398.....	22.2	59.6, 5.4	19.5	8.3, 0.75	0.81
NGC 2217[b].....	...	..., ...	21.8	21.6, 1.72	...
NGC 4440.....	21.2	18.3, 2.2	20.0	4.8, 0.58	0.64
NGC 4643.....	21.9	34.1, 2.1	21.5	19.7, 1.18	1.94
NGC 4650.....	(21.3)	35.4, 6.2	(18.6)	2.8, 0.49	0.38
NGC 4665.....	21.3	32.8, 2.4	22.0	19.1, 1.42	0.74

[a] Decomposition was done based on the azimuthally averaged profiles.
[b] Decomposition was not done for NGC 2217, because of the presence of outer ring.

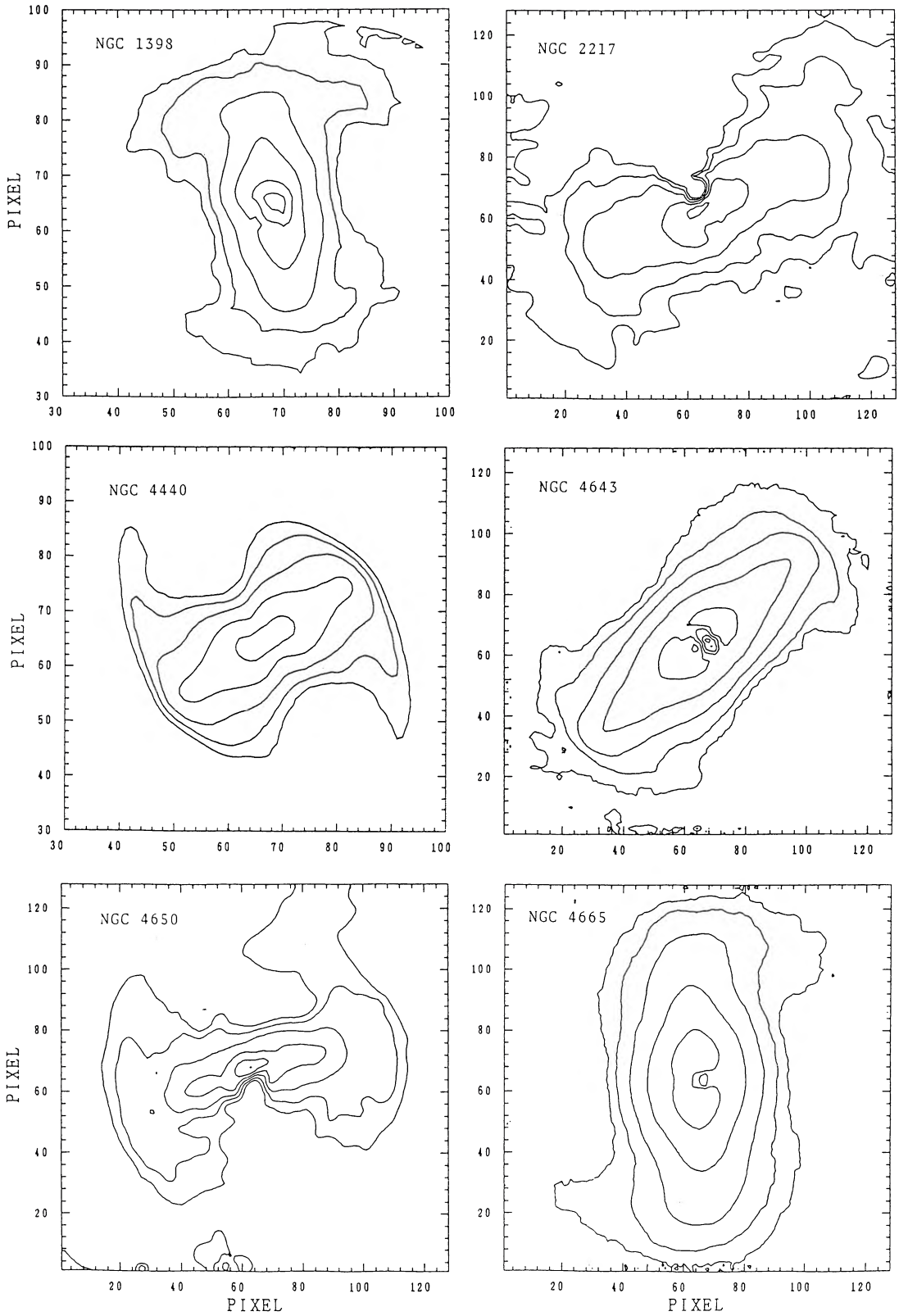

FIG. 9.—Isophotal maps of the extracted bars, i.e., the processed images after subtraction of the axisymmetric components (see the text for the details). The outermost contour is at 25.0 mag arcsec^{-2}, and the interval is 1.0 mag arcsec^{-2}. North is at the top and east is at the left. Pixel size is the same as that of the original image (Fig. 2).

change the initial radial mass distribution into those of Freeman's type I disk. In this case, the problem for the origin of barred spiral galaxies could reduce to the origin of such disks of a peculiar radial mass distribution. In the former case, however, the problem could not be attributable to the difference in the initial radial mass distribution of disks destined to ordinary spirals or barred spirals.

V. LUMINOSITY DISTRIBUTION OF THE BAR ITSELF

a) Extraction of Luminosity Distribution of the Bar Itself

As can be seen from Figure 3, the interbar regions on the azimuthal profiles are broad and nearly flat, whereas the bar regions protrude prominently above them as sharp and narrow humps. Hence, the bar appears as a nonaxisymmetric component superposed on the underlying axisymmetric component. In other words, the disks of barred spiral galaxies can be decomposed expediently into two components, i.e., an axisymmetric component and a nonaxisymmetric component. From the physical point of view, there may be no axisymmetric component on the disks of real barred spiral galaxies, because stellar orbits must deviate significantly from circular orbits by the presence of a bar potential. As shown below, however, this decomposition can extract the bar and other nonaxisymmetric components explicitly.

Simple subtractions of axisymmetric components, expressed by the bar minor axis profiles, from the original images of the galaxies, do not appropriately reproduce the luminosity distributions of the bars themselves for the radii smaller than the bar widths $w_{\rm bar}$, because the bar minor axis profiles in these regions are contaminated by the light of the bar components. To recover this problem, we decompose as follows. After the above processing, the resultant images are fitted to a bar model with a luminosity distribution expressed by equation (2) described in § V*b*. The images are fitted well to this model except for both the nuclear regions and the sector regions where the bar minor axis profiles are derived. Using the processed images after subtracting this bar model from the original images of the galaxies, we again construct the bar minor axis profiles in the same way as done in § IV. This revised profile should be contaminated little from the bar light even at the radius smaller than the bar width. Substracting the revised axisymmetric components, expressed by these revised profiles, from the original images of the galaxies, we finally obtain the nonaxisymmetric components themselves. We refer to them hereafter as the extracted bars. Contour maps of the resulting images are shown in Figure 9. It is noted that the basic features of the images do not change significantly any more, even if we repeat these procedures iteratively.

Except for the nuclear regions, where subtraction of the bulge components is still inappropriate due to slight deviation from axisymmetry and the steep luminosity gradient, these contours reproduce the luminosity distributions of the bar components properly. Aside from the obvious arm or ring structures, the shape of contours at the faint levels appears not as an elliptical but as a rectangular shape with a nearly constant width along the major axis of the bar.

b) Luminosity Profiles along and across the Bar Major Axis

The luminosity profiles along the major axes of the nonaxisymmetric components, i.e., the extracted bars, are shown in Figure 10. Horizontal and short vertical lines in each panel represent the bar region defined in § III*d* and the radius corresponding to the bar width, $w_{\rm bar}$, respectively. In the bar regions, the luminosity profiles are nearly straight, and therefore they follow the exponential distribution. The gradients of the profiles are nearly zero or as much as those of the outer disks of the original images (Fig. 8). For NGC 2217 and NGC 4650, the profiles are almost flat, and the surface brightness changes about 0.1 mag arcsec^{-2} throughout the bar regions, whereas in the steepest case of NGC 4665, it changes nearly 2.5 mag arcsec^{-2}.

We estimated the central surface brightness of the bar $\mu_{0,c}$ by extrapolating the profile to $r = 0$. The mean value is $\mu_{0,c} = 20.9 \pm 0.6$ (1 σ) mag arcsec^{-2} for the five program galaxies excluding NGC 4650, and it is slightly brighter than 21.65 mag arcsec^{-2}, the mean central surface brightness of the exponential disks of spiral galaxies obtained by Freeman (1970). At the bar end zones, the surface brightness decreases very steeply. Beyond the bar ends, there remain the nonaxisymmetric components. As discussed in § III*c*, these are caused by the presence of arms (NGC 1398, NGC 4650), an outer ring (NGC 2217), or tightly wound arms (NGC 4643), and they also may be caused by the influence of the presence of the bar.

Figure 11 shows the luminosity profiles of the extracted bars scanned parallel to the bar minor axis at four bar-dominated radii. Except for the asymmetric features due to the arms or rings as seen in the outskirts of the profiles of NGC 1398 and NGC 4650, each profile is fitted to a Gaussian around the peak and to an exponential in the outskirts of some profiles. Here we adopt a Gaussian function to fit the profiles. As expected from the rectangular shapes of the isophotes (Fig. 9), the scale lengths are found to be nearly constant along the bar for each object. After all, the extracted bar component can be expressed by the equation

$$\mu(x, y) = \mu_{0,c} \exp(-x/x_0) \exp[-(y/y_0)^2], \quad (2)$$

where x and y are the orthogonal coordinates centered at the nucleus and set parallel to the major and minor axes of the bar and $\mu_{0,c}$ is the inclination corrected surface brightness at the center of galaxy ($x = y = 0$). Of course, we should introduce a cutoff radius $x = r_{\rm bar}$ at the bar end. The fitting parameters are summarized in Table 6. This equation was originally proposed by Blackman (1983) for the late-type barred spiral galaxy NGC 7479 (SBc). He fitted it not to the extracted bar, but to an observed image.

To represent the space density distribution of the bar, the equation

$$\rho = \rho_0[1 - (x/a)^2 - (y/b)^2 - (z/c)^2]^n, \quad (3)$$

is frequently used by many authors (de Vaucouleurs and

TABLE 6

PARAMETERS FOR LUMINOSITY DISTRIBUTION OF EXTRACTEED BARS[a]

Object	$\mu_{0,c}$ (mag arcsec^{-2})	x_0	y_0
NGC 1398.....	21.2	48″.8	12″.3
NGC 2217.....	21.4	146	13.8
NGC 4440.....	21.5	50	6.4
NGC 4643.....	20.4	34.1	12.1
NGC 4650.....	(21.4)	200	7.2
NGC 4665.....	19.9	19.1	14.5

[a] The luminosity distribution of the extracted bars are approximated by eq. (2).

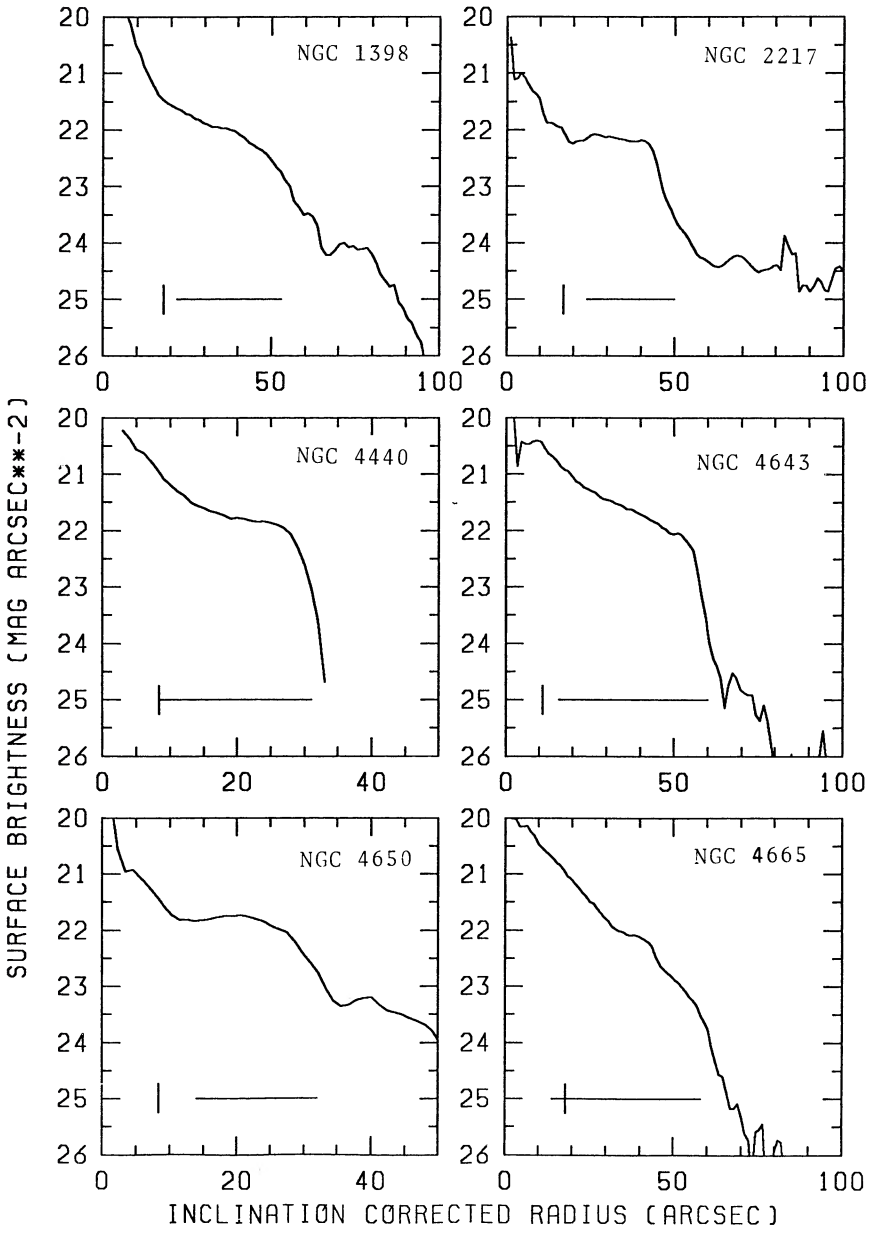

FIG. 10.—The luminosity profiles along the major axes of the extracted bars are given against the inclination-corrected radius. Horizontal and short vertical lines indicate the bar regions and the bar widths defined in § III*d*, respectively.

Freeman 1972; Sanders and Tubbs 1980; Schempp 1982; Teuben and Sanders 1985; Schwarz 1985). The projected luminosity distribution of this model fits well along the major axis of the extracted bar with free parameters of ρ_0 and n (a and b are determined from photometry and c is assumed to be equal to b), but across the bar it fits very poorly; on the profiles parallel to the minor axis, the model yields too flat a ridge around $y = 0$ and too sharp a cutoff around the edge $y = b$. Hence, equation (3) is a poor representation of the barred structure.

c) *Luminosity Fraction of the Bar*

We estimate the luminosity fractions of the bar components. The total luminosity in the annulus $r_{\rm bulge} < r < r_{\rm bar}$, as well as the luminosity of the extracted bar in the same annulus, is derived by integrating the intensities numerically. Note that they are influenced little by the contamination of the bulge light or by the shape of the distribution of bar light in the bulge region. The resulting fraction $f_{\rm bar}(r_{\rm bulge} < r < r_{\rm bar})$ for each galaxy is listed in Table 4, and it ranges from 27% (for NGC 1398) to 48% (NGC 4665).

EE estimated the luminosity fraction of the bar adopting $I_0(r) - I_2(r) + I_4(r)$ as the bar minor axis profile and therefore as the profile for axisymmetric underlying component. We modified their definition of the fraction, by introducing the $m = 6$ component, as

$$f_{\rm bar}(r_{\rm bulge} < r < r_{\rm bar}) = \langle I_2/I_0 \rangle - \langle I_4/I_0 \rangle + \langle I_6/I_0 \rangle , \quad (4)$$

where $\langle I_m/I_0 \rangle$ is the radially averaged relative Fourier ampli-

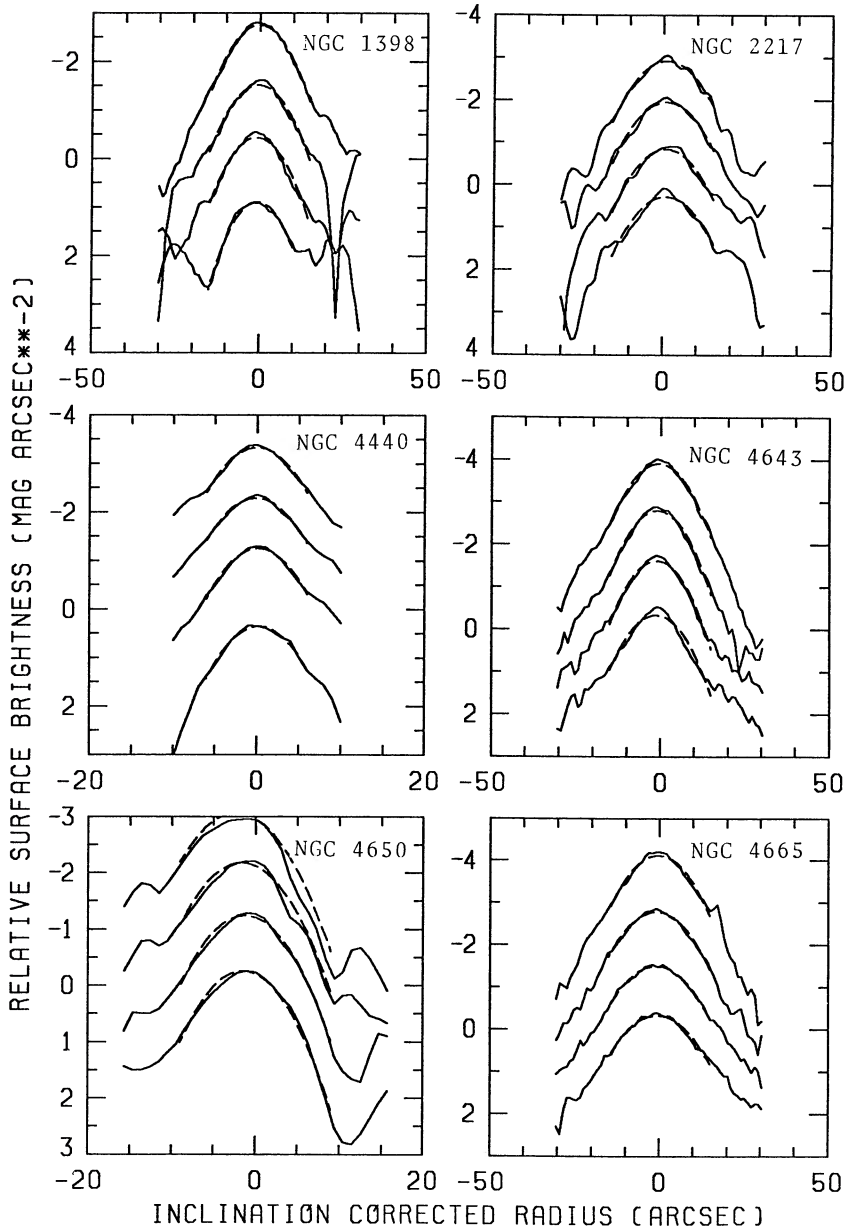

FIG. 11.—The profiles of the extracted bars scanned parallel to the bar minor axis (*solid lines*) are shown at four bar-dominated radii. Dashed lines show the best-fit Gaussian distributions in the fitting ranges.

tude. This equation yields the fractions close to those given in Table 4.

We also estimated the luminosity fractions of the bars with another manner. Calculating the total luminosities of the extracted bars, we obtained the luminosity fractions of the bars within the corrected bar radii $f_{\rm bar}(r < r_{\rm bar})$. They range from 24% (NGC 2217) to 47% (NGC 4665), and they agree with those in Table 4 within factors of 0.8–1.0 for each galaxy, but within a factor of 1.6 for NGC 1398. From the total luminosities contained within R_{25}, we derived the luminosity fractions of the bars against the total luminosities within R_{25}. The resulting values $f_{\rm bar}(r < R_{25})$ are given in the last column of Table 4. The values range from 11% (NGC 4650) to 31% (NGC 4665), and they are as large as those estimated in previous studies for five other SB0 and SBa galaxies (Crane 1975; Benedict 1976; Okamura 1978; EE).

VI. DISCUSSION

a) Summary of the Observational Properties

We summarize the observed properties of the barred spiral galaxies. They will be compared with the properties of bars modeled in N-body simulations in the subsequent subsections.

1. The barred spiral galaxies can be decomposed into the axisymmetric component and the nonaxisymmetric component, i.e., the bar component. The radial luminosity profile of the axisymmetric component is expressed by the bar minor axis profile, which has a prominent dip as like Freeman's type II profile.

2. On the azimuthal profiles, the bars appear as narrow humps superposed on the broad nearly flat parts (axisymmetric components). The luminosity contrasts between the bars and interbars are surprisingly large, 2.5–5.5, which implies

that the bar components should not be treated as perturbing components in the study of its kinematics. Fourier decompositions of the azimuthal profiles show that the largest contribution comes from the $m = 2$ component ($I_2/I_0 = 0.5$–0.7), but higher even-order components are unexpectedly large. In particular, the contributions from the $m = 4$ and $m = 6$ components amount to 0.5 and 0.3 of that of $m = 2$, respectively.

3. The bar major axis profiles protrude prominently in the bar regions above the extrapolated straight lines of the outer exponential disks, and at the bar ends the surface brightness decreases sharply with the e-folding linear scales ranging from 420–1700 pc. On the other hand, the bar minor axis profiles have prominent dips like Freeman's type II profiles.

4. The azimuthally averaged luminosity profiles, however, merge continuously into the outer exponential disks with no luminosity jumps at the bar ends, except for NGC 2217 which has a prominent outer ring. Hence, the azimuthally averaged profiles are of Freeman's type I profile and so are indistinguishable from those of ordinary spirals. The parameters describing exponential disks (r_0, $B(0)_c$) and $r^{1/4}$-law bulges (r_e, μ_e) are not different systematically from those of ordinary spirals.

5. The ratios $r_{\rm bar}/r_0$ and $r_{\rm bar}/R_{25}$ lie in the ranges of 0.9–1.8 and 0.24–0.59, respectively, where $r_{\rm bar}$, r_0, and R_{25} refer to bar radius, scale length of the outer exponential disk, and radius at $\mu_B = 25.0$ mag arcsec^{-2} in RC2 (*ESO/Uppsala Catalogue* for NGC 4650), respectively.

6. The ridges of the bars along the major axes are found to delineate an exact straight line; no deviations from a straight line are found with a detection limit of $\Delta\theta = 1°$–$2°$. Between the leading and trailing sides of the bars, no systematic difference in the luminosity larger than 5%–10% is detected. Hence, the bars are highly symmetric with respect to the ridge of the bar.

7. The luminosity fractions of the bars over the disks within the annulus bounded by $r_{\rm bulge}$ and $r_{\rm bar}$ are 27%–48%, and those over the total luminosities inside R_{25} are 11%–31%.

8. The bar components are extracted as nonaxisymmetric components by subtracting the underlying axisymmetric components from the original images. The shapes of isophotes at the faint levels of the extracted bars are not elliptical but rectangular. The axial ratios of bars defined as $r_{\rm bar}/w_{\rm bar}$ are 0.18–0.34.

9. The luminosity distributions along the major axes of the extracted bars are exponential type, and the gradients are nearly zero or at most as steep as those of the outer exponential disks. The surface brightnesses of the ridges of the bars change only about 0.1 mag arcsec^{-2} in the flat cases and about 2.5 mag arcsec^{-2} in the steepest case throughout the bar regions.

10. The luminosity distributions across the extracted bars are expressed by a Gaussian function with a nearly constant scale length along the bar major axis for each bar.

b) Comparison with N-Body Simulation

N-body simulations of stellar disks reveal formation of a bar as a result of bar instability (e.g., Hohl 1971). Since the shapes of these bars apparently resemble the observed bars, they often become a subject of discussion in regard to the bar formation in barred spiral galaxies. In this subsection, we compare the structure of the bar formed in N-body simulation with those of the observed bars quantitatively.

The results of N-body simulations were kindly provided by M. Noguchi, and the details of the model were described in his paper (Noguchi 1987). Although Noguchi (1987) studied the bar formation process during galaxy interactions, the bar in the present model is formed not as a result of a tidal interaction but of the bar instability in a stellar disk, because the simulation was made with a massless perturber. The initial conditions of his simulation are described briefly below. The disk consists of 20,000 particles having an initial surface mass density of an exponential law with a cutoff at the radius equal to one-fourth of the frame size. The disk is surrounded by a spherical halo of the same mass as the disk so as to yield a flat rotation curve. The velocity dispersion of the disk is taken to be $Q = 1$ (Toomre's Q value). The calculations were made with a cloud-in-cell method with 64×64 meshes and were stopped at 15 galactic rotations.

After a few galactic rotations, a steady bar was formed as in the cases of Hohl (1971, 1976) and Combes and Sanders (1981). The analysis of this model for a barred spiral galaxy is similar to that applied to the present surface photometry. In order to improve the poor signal-to-noise ratio due to a small number of particles in a single frame, we composed five successive frames obtained along a time sequence and subdivided the resultant frame into 512×512 pixels for the convenience of calculations. The contour map of the N-body bar, after smoothing with a Gaussian beam, is shown in Figure 12 for the region within the bar radius. Unlike the observed bars, the shape of the bar is close to an ellipse.

As can be seen from Figure 13, the azimuthal profiles at the bar region ($r = 33$–76) look like a sinusoidal curve and differ significantly from those of observed bars (Fig. 3). The difference of the light (mass) distribution of the bar is also seen in the radial variation of the relative amplitudes of Fourier components (Fig. 14). In the bar region, only the $m = 2$ and $m = 4$ components are prominent, and other even-order components higher than $m = 6$ are as small as those of the noise level. The

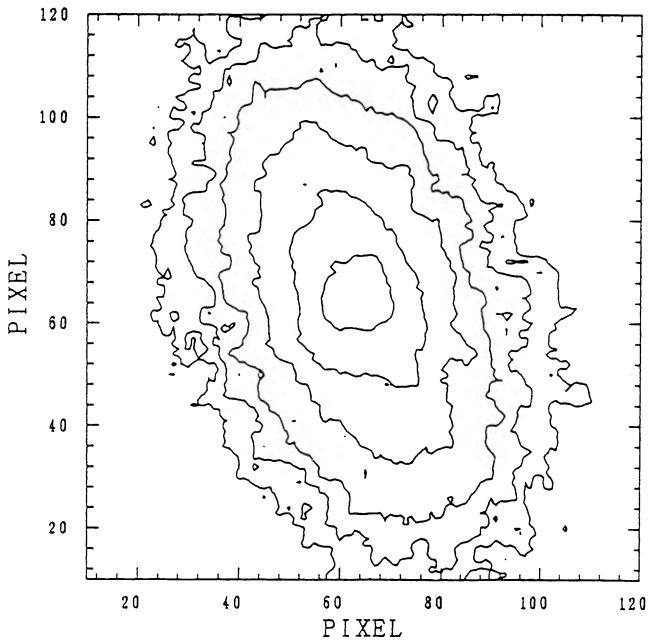

FIG. 12.—Isophotal map of the bar formed in the N-body numerical simulation made by Noguchi. The contour levels are presented in magnitude scale with a interval of 0.5 mag. The interval of large tick marks on the border is 20 pixels. Smoothing is made with running mean of 5×5 pixels for clear representation.

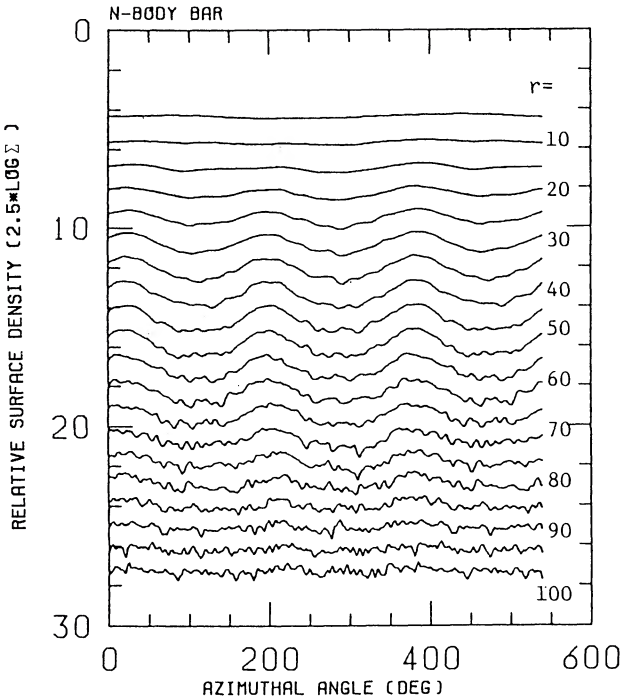

FIG. 13.—Azimuthal profiles of the N-body bar. The radius for each profile is given at the right end of the profile. A total of 1.5 cycles are shown. Humps corresponding to the bar are broader than those in observed galaxies (see Fig. 3).

ratio I_4/I_2 is less than the value 0.5 obtained in § III*c* for the present program galaxies.

The symmetry of the barred structure was examined in the same way as in §§ III*f* and III*g*. The angular separations of peaks on the azimuthal profiles are not exactly 180° as in the case of the observed bars; the standard deviation from 180° is 7°. The degree of the symmetry with respect to the bar major axis is slightly worse than that in the observed bars; the contribution from the antisymmetric part amounts to 5%–10%. Such asymmetry is probably caused by the statistical fluctuation with a small number of particles. Thus simulations with a larger number of particles may improve the degree of symmetry.

In Figure 15, the radial variations of the luminosity contrast between the bar and the interbar are presented in two ways as shown in Figure 5. Similar to the observed bars, the contrast rises first, reaches the peak value at the middle of the bar, and finally decreases as the radius increases. The maximum contrast in the dashed curve is ~ 3.3, and this is comparable to the observed values. The bar radius, $r_{\rm bar}$, and the bar width, $w_{\rm bar}$, derived from Figures 15 and 13, respectively, with the same definition in § III*d* are 76 and 33, respectively. The bar widths vary with the radius, and so we adopted the averaged value. The derived axial ratio 0.43 is larger than the largest value of the observed bars.

Three kinds of radial luminosity profiles are shown in Figure 16. A horizontal line in the figure shows the bar region which is bounded by $r_{\rm bar}$ and $w_{\rm bar}$. The bar major axis profile has following two important properties which are quite different from those in observed bars: (i) the gradient of the profile is much steeper in the bar region than in the outer disk region, and (ii) there is no sharp cutoff at the bar end. As for the bar minor axis profile and the azimuthally averaged profile, they look similar to the observed profiles (Fig. 8). However, the steep rise of the profiles inside $r = 70$ is not due to the presence of a spherical bulge, because the present simulation does not include a bulge component. Since the initial surface density distribution is given by the exponential law, this steep rise of the azimuthally averaged profile inside $r = 70$ indicates an occurrence of a radial mass flow during the bar formation process.

Beyond the bar radius, the three radial profiles merge each other into the exponential disk. This means that the structure in the outer disk is not distorted by the presence of the bar. We derived the scale length r_0 of the exponential disk in this region. The ratio $r_{\rm bar}/r_0$ is 1.6, which is comparable to the values for NGC 4440, NGC 4643, and NGC 4665.

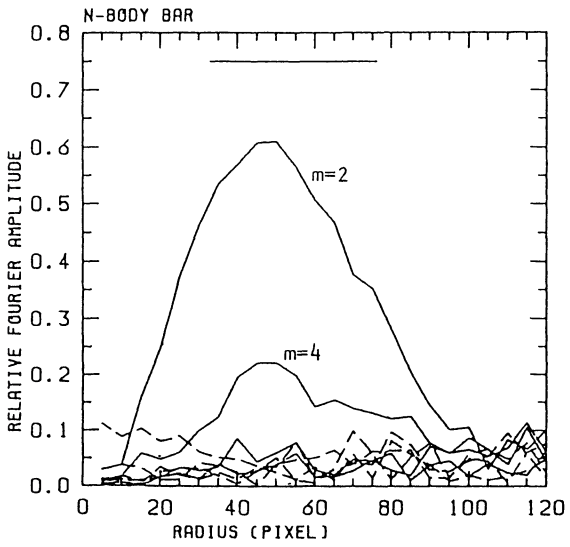

FIG. 14.—Relative amplitudes of Fourier components (I_m/I_0; $m = 1, \ldots, 8$) of the N-body bar are given as a function of radius. Solid lines and dashed lines show even and odd components, respectively. Horizontal line indicates the bar region bounded by $r_{\rm bar}$ and $w_{\rm bar}$.

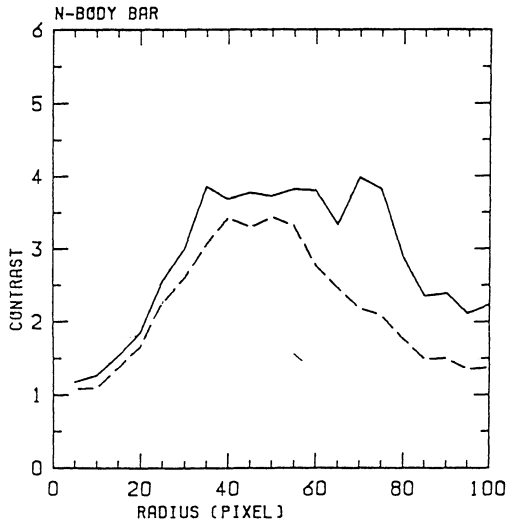

FIG. 15.—Surface density contrast between the bar and the interbar of the N-body bar. The analysis was done similarly as in the case of Fig. 5. Solid line shows the ratio of the peak surface density to the bottom surface density of the azimuthal profiles. Dashed line shows the ratio of $(I_0 + I_2 + I_4 + I_6)$ to $(I_0 - I_2 + I_4 - I_6)$, where I_m is a Fourier amplitude of mth component.

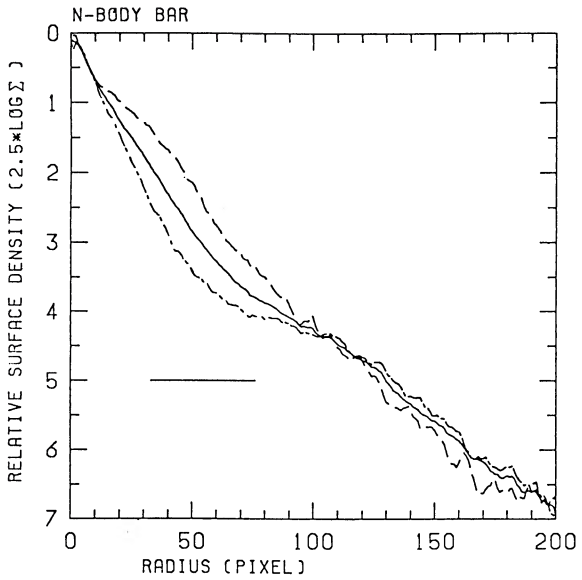

FIG. 16.—The radial surface density profiles of the N-body bar along the bar major axis (*dashed line*) and bar minor axis (*dash-dotted line*), and azimuthally averaged (*solid line*) profiles. Horizontal line indicates the bar region bounded by r_{bar} and w_{bar}.

The luminosity distribution across the bar is almost Gaussian, and the scale length of a Gaussian distribution increases as the radius increases contrary to the observed bars. The luminosity fraction of the bar in the annulus bounded by w_{bar} and r_{bar} is obtained from equation (4) using the Fourier amplitudes and the result is 39%, which is comparable to those of observed barred spiral galaxies.

At a glance, the N-body bar is reminiscent of observed bars in its appearance, but quantitatively, the properties of the surface density distribution are quite different from those of observed ones.

c) *Comparison with Other Simulations*

We should examine whether the above properties of the present simulation model are common to those of other simulations done under different initial conditions.

Hohl (1971) simulated the evolution of a stellar disk with an initial surface density distribution given by $\mu(r) = \mu(0)(1 - r^2/a^2)^{1/2}$ (Maclaurin disk). Thielheim and Wolff (1984) studied the disk of $\mu(r) = \mu(0)(1 + r^2/a^2)^{-3/2}$ (Toomre's model 1), which is surrounded by a spherical halo of $\rho(r) = \rho(0)(1 + r^2/b^2)^{-5/2}$. Toomre's model 1 disk, with a vertical mass distribution given by $\mathrm{sech}^2\ (z/z_0)$ and surrounded by a spheroidal halo, was studied by Combes and Sanders (1981). Like the present Noguchi model, the above three simulations show that after a few galactic rotations a bar is formed and that it soon becomes a steady state. Their azimuthal profiles in the bar regions look like a sinusoidal curve. The azimuthally averaged profiles are approximated by two straight lines of different gradient, i.e., steep in the inner region while shallow in the outer region. The bar lies in the inner steep region. The bar major axis profile is also approximated by two straight lines with different gradient and has no sharp cutoff at the bar end. The bar minor axis profile is like Freeman's type II disk, although no bulge component exists. All these properties are common to those of the present simulation model.

Three-dimensional N-body simulations dealing with the collapse of a stellar system also show a bar structure (Miller and Smith 1979; Hohl and Zang 1979). The azimuthal profiles in the bar region given by Hohl and Zang (1979, model IV, Fig. 12 in their paper) look like a superposition of narrow humps on a nearly flat component, similarly to our observations. But the surface density contrast between the ridge of the bar and the bottom of the interbar is about 7, which is larger than the observed values 2.5–5.5. The density span along the radius in the bar region is more than ~ 5 mag, as in the case studied by Miller and Smith (1979). This is much larger than the observed span (0.1–2.5 mag arcsec^{-2}). The sharp density cutoff is not seen at the bar ends in both simulations. Thus, the properties of these simulations are basically similar to those of the present simulation.

Do the above properties of N-body bars change significantly if a bulge component is included in simulations? Hohl (1978) studied the effects of a nuclear bulge. In his two-dimensional simulation, the azimuthally averaged profile falls steeply in an inner region as the radius increases. It gets slightly flattened around the bar end and falls steeply again beyond the bar end. However, in his three-dimensional simulation, the disk remains stable and shows no barred structure. Its azimuthally averaged profile follows the exponential law. Expressing a nuclear bulge with a Plummer sphere, Sparke and Sellwood (1987) made two-dimensional N-body simulations. The bar major axis profile in the bar region of their simulation is not as flat as that of the observed bars. At present, the effects of a nuclear bulge on the structure and formation of bars are not well known, and further simulations are necessary to clarify them (Sellwood 1985, 1989; Nishida 1986; Hozumi, Fujiwara, and Nishida 1987).

Pence and de Vaucouleurs (1985) made a surface photometry of NGC 4027, a late-type barred spiral galaxy (SBdm) with a small nuclear bulge, and they found that the gradient of luminosity profile along the major axis of the bar is steep inside the bar radius, while less steep outside of it. Similar result is obtained by Blackman (1983) for NGC 7479 (SBc). This feature well resembles to the result of the numerical simulation shown in Figure 16, which was done without a spherical bulge component. In order to examine the differences of the bar structure between early-type and late-type barred spiral galaxies, an examination of whether the above feature of NGC 4027 and NGC 7479 is common for all late-type barred spiral galaxies with small nuclear bulges is urgently needed.

We are grateful to M. Noguchi for providing us the results of N-body simulations and R. Kennicutt for loan of Swope telescope plates. We also acknowledge T. Ishizawa, M. T. Nishida, M. Noguchi, S. Okamura, and M. Sasaki for helpful discussions. We thank the staff members of the Kiso observatory for their assistance in the data reduction. K. Ohta wishes to thank Professor M. Saitō for his continuous encouragement. The data analysis was carried out with Facom S-3500 at the Kiso observatory and Facom M780 at the Data Processing Center of Kyoto University.

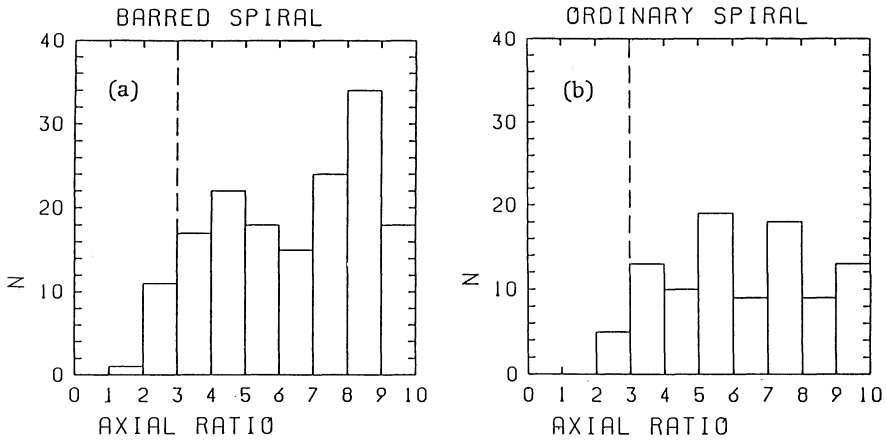

FIG. 17.—Histograms for the apparent axial ratios for (*a*) 160 barred spiral galaxies and (*b*) 96 ordinary spiral galaxies. The data were taken from RC2.

APPENDIX

ON THE CIRCULAR SYMMETRY OF THE OUTER DISKS OF BARRED SPIRAL GALAXIES

For ordinary spiral galaxies, faint outer disks are believed to be circular symmetric. For barred spiral galaxies, however, even the outer disks far beyond the end of the bars could be distorted by the presence of the bar. Thus we should check the assumption, adopted for determination of galaxy inclination, that outer disks of barred spiral galaxies are circular symmetric.

In Figures 17*a* and 17*b*, histograms of axial ratios are shown for barred spiral galaxies and ordinary spiral galaxies, respectively. The axial ratios and morphological data are taken from RC2. We selected 160 barred spirals which are morphologically classified as SB0/a to SBab but not assigned a code P (peculiar). As a control sample, we took 96 ordinary spirals with morphological types S0/a to Sab without a code P (peculiar). If the disks in the faint outer regions are intrinsically circular symmetric and are distributed randomly to the line of sight, then the distribution should be flat in the histograms. Galaxies with an axial ratio less than 0.3 should be rejected, because these galaxies are so highly inclined that it is difficult to comment on the presence or absence of the bars, and their axial ratios do not represent actual inclinations owing to the finite thickness of the disks. As expected, Figures 17*a* and 17*b* show uniform distributions of the ratios for both ordinary and barred spirals. The χ^2 values are 11.77 and 7.85 for barred spirals and ordinary spirals, respectively. Hence, the null hypothesis that the structure of outer disks of barred spirals is circular is not rejected at 5% level of significance.

REFERENCES

Baumgart, C. W. 1983, Ph.D. thesis, University of Missouri.
Benedict, G. F. 1976, *A.J.*, **81**, 799.
Binggeli, B., Sandage, A., and Tammann, G. A. 1985, *A.J.*, **90**, 1681.
Blackman, C. P. 1983, *M.N.R.A.S.*, **202**, 379.
Boroson, T. 1981, *Ap. J. Suppl.*, **46**, 177.
Bottinelli, L., Gouguenheim, L., Paturel, G., and de Vaucouleurs, G. 1983, *Astr. Ap.*, **118**, 4.
———. 1984, *Astr. Ap. Suppl.*, **56**, 381.
———. 1985, *Astr. Ap. Suppl.*, **59**, 43.
Burstein, D. 1979, *Ap. J.*, **234**, 435.
Buta, R. 1986*a*, *Ap. J. Suppl.*, **61**, 609.
———. 1986*b*, *Ap. J. Suppl.*, **61**, 631.
———. 1987, *Ap. J., Suppl.*, **64**, 383.
Buta, R., and de Vaucouleurs, G. 1983, *Ap. J. Suppl.*, **51**, 149.
Combes, F., and Sanders, R. H. 1981, *Astr. Ap.*, **96**, 164.
Crane, P. 1975, *Ap. J.*, **197**, 317.
de Vaucouleurs, G. 1963*a*, *Ap. J.*, **137**, 720.
———. 1963*b*, *Ap. J. Suppl.*, **8**, 31.
———. 1963*c*, *Ap. J.*, **138**, 934.
———. 1975, *Ap. J. Suppl.*, **29**, 193.
de Vaucouleurs, G., de Vaucouleurs, A., and Corwin, H. G., Jr. 1976, *Second Reference Catalogue of Bright Galaxies* (Austin: University of Texas Press) (RC2).
de Vaucouleurs, G., and Freeman, K. C. 1972, *Vistas Astr.*, **14**, 163.
Duval, M. F., and Athanassoula, E. 1983, *Astr. Ap.*, **121**, 297.
Duval, M. F., and Monnet, G. 1985, *Astr. Ap. Suppl.*, **61**, 141.
Elmegreen, B. G., and Elmegreen, D. M. 1985, *Ap. J.*, **288**, 438 (EE).
Freeman, K. C. 1970, *Ap. J.*, **160**, 811.
Hohl, F. 1971, *Ap. J.*, **168**, 343.
———. 1976, *A.J.*, **81**, 30.
———. 1978, *A.J.*, **83**, 768.
Hohl, F., and Zang, T. A. 1979, *A.J.*, **84**, 585.
Hozumi, S., Fujiwara, T., and Nishida, M. T. 1987, *Pub. Astr. Soc. Japan*, **39**, 447.
Hubble, E. 1926, *Ap. J.*, **64**, 321.
Ichikawa, S. 1987, *Ann. Tokyo Astr. Obs.*, 2nd Ser., **21**, 437.
Ichikawa, S., Okamura, S., Watanabe, M., Hamabe, M., Aoki, T., and Kodaira, K. 1987, *Ann. Tokyo Astr. Obs.*, 2nd Ser., **21**, 285.
Kent, S. M. 1985, *Ap. J. Suppl.*, **59**, 115.
King, I. R. 1978, *Ap. J.*, **222**, 1.
Kodaira, K., Watanabe, M., and Okamura, S. 1986, *Ap. J. Suppl.*, **62**, 703.
Kormendy, J. 1983, *Ap. J.*, **275**, 529.
Lauberts, A. 1982, *The ESO/Uppsala Survey of the ESO(B) Atlas* (München: European Southern Observatory).
Longo, G., and de Vaucouleurs, A. 1983, *A General Catalogue of Photoelectric Magnitudes and Colors in the U, B, V System of 3,578 Galaxies Brighter than the 16-th V-magnitude (1936–1982)* (Austin: University of Texas Press).
Lynden-Bell, D. 1979, *M.N.R.A.S.*, **187**, 101.
Matsuda, T., Inoue, M., Sawada, K., Shima, E., and Wakamatsu, K. 1987, *M.N.R.A.S.*, **229**, 295.
Miller, R. H., and Smith, B. F. 1979, *Ap. J.*, **227**, 785.
Nishida, M. T. 1986, *Ap. J.*, **302**, 611.
Noguchi, M. 1987, *M.N.R.A.S.*, **228**, 635.
Okamura, S. 1978, *Pub. Astr. Soc. Japan*, **30**, 91.
———. 1988, *Pub. A.S.P.*, **100**, 524.
Ostriker, J. P., and Peebles, P. J. E. 1973, *Ap. J.*, **186**, 467.
Palumbo, G. G. C., Tanzella-Nitti, G., and Vettolani, G. 1983, *Catalogue of Radial Velocities of Galaxies* (New York: Gordon and Breach).
Pence, W. D., and de Vaucouleurs, G. 1985, *Ap. J.*, **298**, 560.
Petrou, M. 1984, *M.N.R.A.S.*, **211**, 1p.
Sandage, A. 1961, *The Hubble Atlas of Galaxies* (Washington, DC: Carnegie Institution of Washington).
Sanders, R. H., and Tubbs, A. D. 1980, *Ap. J.*, **235**, 803.
Schempp, W. V. 1982, *Ap. J.*, **258**, 96.
Schwarz, M. P. 1981, *Ap. J.*, **247**, 77.
———. 1984, *M.N.R.A.S.*, **209**, 93.
———. 1985, *M.N.R.A.S.*, **212**, 677.
Sellwood, J. A. 1980, *Astr. Ap.*, **89**, 296.

Sellwood, J. A. 1981, *Astr. Ap.*, **99**, 362.
———. 1985, *M.N.R.A.S.*, **217**, 127.
———. 1989, *M.N.R.A.S.*, **238**, 115.
Sørensen, S.-A., Matsuda, T., and Fujimoto, M. 1976, *Ap. Space Sci.*, **43**, 491.
Sparke, L. S., and Sellwood, J. A. 1987, *M.N.R.A.S.*, **225**, 653.
Teuben, P. J., and Sanders, R. H. 1985, *M.N.R.A.S.*, **212**, 257.
Thielheim, K. O., and Wolff, H. 1984, *Ap. J.*, **276**, 135.
van Albada, G. D., and Roberts, W. W., Jr. 1981, *Ap. J.*, **246**, 740.
Visvanathan, N., and Griersmith, D. 1979, *Ap. J.*, **230**, 1.

MASARU HAMABE: Kiso Observatory, Institute of Astronomy, The University of Tokyo, Mitake-mura, Kiso, Nagano 397-01, Japan

KOUJI OHTA: Department of Astronomy, Faculty of Science, Kyoto University, Kyoto 606, Japan

KEN-ICHI WAKAMATSU: Physics Department, College of Technology, Gifu University, Yanagido, Gifu 501-11, Japan